Materials Today Communications 40 (2024) 109826

Contents lists available at ScienceDirect

Materials Today Communications

journal homepage: www.elsevier.com/locate/mtcomm

Targeted lipid-coated ZnO nanoparticles coupled with ultrasound: A sonodynamic approach for the treatment of osteosarcoma as 3D spheroid models

Marco Carofiglio [a], Giulia Mesiano [a], Giada Rosso [a], Marzia Conte [a], Marco Zuccheri [a], Ymera Pignochino [b,c], Valentina Cauda [a,*]

[a] Department of Applied Science and Technology, Politecnico di Torino, C.so Duca degli Abruzzi 24, Turin 10129, Italy
[b] Department of Clinical and Biological Sciences, University of Turin, Regione Gonzole 10, Orbassano, TO 10043, Italy
[c] Candiolo Cancer Institute, FPO-IRCCS, Strada Provinciale 142 Km 3.95, Candiolo, TO 10060, Italy

ARTICLE INFO

Keywords:
ZnO
Sonodynamic therapy
Osteosarcoma
Hybrid nanoparticles
Active targeting
Liposomes

ABSTRACT

Bone cancer is a rare disease with limited treatment options. Surgery and chemotherapy frequently fail to cure the disease because metastases can develop in the former, and the latter often lacks specificity. Innovative therapeutic treatments are therefore needed to address this rare disease, which typically affects children and adolescents. Physical stimulation to remotely activate a therapeutic agent may represent a promising solution, especially for deep-seated and/or distributed tumors. In this regard, sonodynamic therapy gathers importance: it offers a valid solution to the limitations of photodynamic therapy, such as limited tissue penetration, but retains the advantages of remotely activatable cell death. In this work, we developed lipidic coated iron-doped zinc oxide nanoparticles with superior biocompatibility as remotely activated sonosensitizers for osteosarcoma sonodynamic therapy and an active targeting mechanism addressing the erythropoietin-producing hepatocellular receptor-2 overexpressed in bone cancer cells. The positively charged zinc oxide NPs are coated with a negatively charged phospholipidic shell, which significantly enhances the biocompatibility and hemocompatibility of the nanoconstruct. Most importantly, the lipidic shell is modified by grafting a targeting peptide onto it, increasing cellular uptake towards osteosarcoma cells and demonstrating the potential to address various tissues with the same system. Reactive Oxygen Species (ROS) are effectively generated upon ultrasound stimulation and measured through electron paramagnetic resonance spectroscopy. The nanoconstructs are evaluated in vitro on 3D osteosarcoma spheroids, to demonstrate the effectiveness of the combination of NPs and ultrasound stimulation in suppressing the growth of bone osteosarcoma. The biocompatibility, targeting capabilities, and potential flexibility of the nanoparticles here described open up avenues for an effective and remotely-activated cancer therapy.

1. Introduction

Bone tumors are a rare disease, constituting less than 1 % of cancer cases in the elderly population but up 3–5 % of cancer cases in adolescent and children [46]. Osteosarcoma, the most commonly diagnosed malignant bone tumour, presents an average 5-years survival rate of approximately 60 %, which significantly decreases in case of metastases [47]. In most cases, osteosarcoma primarily develops in the upper and lower limbs, and typically, patients eventually end up undergoing leg or arm amputation. Therefore, being able to intervene in a less invasive and drastic manner would greatly improve patients' quality of life. Conventional treatment techniques for this disease typically involve standard surgery and chemotherapy, and, in some cases, radiotherapy. Still, the survival rate has shown limited improvement over the years [47], underscoring the need for innovative approaches to address this challenging disease.

From a purely physical perspective, treating bone osteosarcoma without invasive techniques and avoiding limbs amputation poses a formidable challenge. Since the tumor primarily occurs within the bones, external stimuli - such as light used in photodynamic or

* Corresponding author.
E-mail address: valentina.cauda@polito.it (V. Cauda).

https://doi.org/10.1016/j.mtcomm.2024.109826
Received 4 April 2024; Received in revised form 5 July 2024; Accepted 11 July 2024
Available online 14 July 2024

photothermal therapies - have difficulty reaching the affected area. This limitation persists even when employing high-penetrating wavelengths like infrared light, which however can only penetrate the body to a depth of a few millimetres [60].

Ultrasound exploiting therapies have the potential to overcome these penetration issues [41]. Acoustic waves can effectively penetrate soft tissues and either generate heat to ablate the tumor (high intensity focused US, HIFU) [61,67] or induce cavitation onto the target tissue, i.e. the collapse and the subsequent implosion of gas bubbles due to the ultrasound pressure waves with consequent reactive oxygen species (ROS) formation (sonodynamic therapy) [38,45,72]. ROS can induce cell death through oxidative stress and, upon an effective targeting of the phenomenon toward cancerous tissues [68], they can be used to induce tumor suppression [82].

Recent developments have seen sonodynamic therapy coupled with sonosensitizers, both as organic molecules [16,39,40] and inorganic materials [28,29,49,50,71]. Among them, metal oxides nanoparticles play a crucial role.

The most promising ones are surely titanium oxide (TiO_2) [25,29,73,77,80], colloidal gold [6] and zinc oxide (ZnO) [30,43,70] nanoparticles (NPs). TiO_2 and ZnO have been coupled with high pressure waves to induce a cytotoxic effect on tumoral cell lines in 2D in vitro tests [10,51,69]. Still, shock waves have shown little capacity to generate ROS when coupled to the inorganic NPs, mainly relying on mechanical effects to induce cytotoxicity.

Nonetheless, ZnO has been proven to increase ROS generation in liquid media when subjected to standard ultrasound (US) radiation [2,8]. Despite the good premises of ZnO as sonosensitizer, its exploitation has been limited by its dose dependent toxicity in its nanosized form, due to its dissolution in biological media [9,59]. Various techniques have been explored and combined together to increase the biocompatibility of ZnO, to obtain a sonosensitizer that can be safely administered to the diseased tissue and then remotely activated on demand by the ultrasound irradiation.

For example, doping ZnO NPs with iron was proved to reduce the dissolution of the NPs in biological media and to increase their safety toward healthy cells by selectively killing cancer cells [10,76].

Furthermore, the biocompatibility of NPs can be improved through their surface stabilization. Recent trends see the coating of NPs with lipidic bilayers derived from cells or exosomes [20,21,23,31,54], which confer interesting properties in terms of intrinsic targeting capabilities, biocompatibility and low immunogenicity ([78]; Q. [81]). Alternatively, synthetic lipids coatings are much easier to produce on a large scale, they are highly controllable and customizable to specific needs and already widely employed in clinical trials [42]. Targeting molecules can also be chemically conjugated to lipids, turning them into both a shielding moiety and a robust customizable targeting system.

The biocompatibility and effectiveness of these NPs have mainly been tested on 2-dimensional (2D) cell cultures. However, research is rapidly moving toward 3-dimensional (3D) cultures. Indeed, they better represent the biological environment and cell to cell interactions [24]. Furthermore, they can be designed to replicate some of the features that make some tumors difficult to address, mimicking the tumor microenvironments and better simulating the effects of the drugs or nanoparticles on the biological barriers that must be overcome to reach the target tissue [15,66]. Additionally, 3D cell systems gain the advantages of high spatiotemporal resolution, the possibility to control experimental variables and the possibility to perform reverse engineering of the tumor microenvironment, with respect to mice models, resulting in a better understanding of the mechanisms lying aside the biological behaviour [58]. In light of the above, their use has also been highly recommended by both the Food and Drug Administration (FDA) and the European Medicines agency (EMA) in recent mandates (December 2022 and September 2021 respectively) [22] to reduce the employment of animal models in preclinical research.

The importance of 3D models becomes even more pronounced in the case of physical stimuli for therapy activation. Indeed, studying a sonosensitizer requires a deep understanding of how acoustic waves propagate in the target environment. A 2D in vitro model may poorly represents an actual in vivo system in which US waves propagate in three dimensions. The application of US against 3D cells spheroids is a rapidly growing field where drug or drug-carried NPs have been tested [34,35,37,57].

In this study, we prove for the first time the efficacy of iron-doped ZnO (FZ) NPs as sonosensitizing agents for the treatment of bone osteosarcoma in a 3D spheroid model. FZ NPs have been made biocompatible through a smart phospholipidic formulation enabling the bioconjugation of potentially any targeting moiety. In this specific case, we increase the specificity for osteosarcoma cells by incorporating a targeting peptide in the formulation. This peptide recognizes the erythropoietin-producing hepatocellular receptor-2 (EphA2), an oncoprotein that is particularly overexpressed in these tumors [13,27].

We first assessed the biocompatibility and cell internalization of FZ NPs using two different bone osteosarcoma cell lines. The tests involved a comparison between pristine NPs and lipid-coated ones, demonstrating the effectiveness of the lipidic coating in mitigating the dose-dependent toxicity of ZnO NPs. Furthermore, the targeting mechanism was proven to enhance nanoparticle internalization compared to the non-targeted version. The response of FZ NPs to US stimulation was also a focal point of our investigation. We evaluated the generation of high levels of ROS under US exposure of the NPs using electron paramagnetic resonance (EPR) spectroscopy. Subsequently, we tested all three NPs formulations (pristine, lipid-coated, and targeted-lipid coated FZ NPs) on 3D spheroids of bone osteosarcoma in terms of metabolic activity and we further observed NPs internalization using confocal microscopy. The results were then compared to those obtained from EPR spectroscopy to gain a deeper understanding of the potential causes of cell death.

In summary, our study introduces a novel sonodynamic approach for the treatment of bone osteosarcoma, employing a biocompatible sonosensitizer, FZ NPs, that can be remotely activated using safe levels of US. The importance and originality of this study consists in the use of an innovative biomimetic and targeted NPs, demonstrating its effectiveness as a stimuli responsive nanomedicine under acoustic pressure activation. Furthermore, our work illustrates the enhanced safety achieved through the innovative lipidic coating of our metal oxide nanocrystals. This coating finely tuned the interactions of these hybrid nanoparticles with recipient cells, even in 3D models, resulting in rapid and efficient internalization and intracellular biodistribution.

2. Materials and methods

2.1. Iron-doped ZnO NPs (FZ NPs) synthesis

Iron-doped zinc oxide nanoparticles (FZ NPs) were synthetized following a method previously optimized in our laboratory [11]. Specifically, 526 mg of zinc acetate dihydrate ($Zn(CH_3COO)_2{\cdot}2\ H_2O$, Sigma-Aldrich) was dissolved in 40 mL of absolute ethanol (99 %, Sigma-Aldrich). Subsequently, 58 mg of ferric nitrate nonahydrate ($Fe(NO_3)_3{\cdot}9\ H_2O$, HiMedia), corresponding to 6 % of the Fe/Zn ratio, was added to the solution. The solution was vigorously stirred at 70 °C to ensure complete dissolution of the salts. After 5 minutes, 140 μL of oleic acid (≥99 %, Sigma-Aldrich) and 1 mL of bidistilled water (b.d., obtained from a Direct Q3 system, Millipore) was added to the solution, which was left under moderate stirring.

Separately, an ethanolic solution of tetramethylammonium hydroxide pentahydrate (TMAH, 98.5 %, Sigma-Aldrich) was prepared by dissolving 1.044 g of TMAH in 10 mL of ethanol and 1.052 mL of water. This solution was then rapidly poured in the zinc precursor solution to initiate particle condensation. After 10 minutes of stirring at 70°C, 40 mL of ice-cooled ethanol was added to the solution to halt the reaction. The resulting particle dispersion was collected and washed three times with ethanol using repeated centrifugations (10 minutes at

8000 g) and redispersions.

The obtained FZ NPs were further functionalized with amino groups to successively enable the attachment of dyes for in vitro applications. In detail, 40 mg of FZ NPs was suspended in ethanol at a concentration of 2.5 mg/mL. The solution was nitrogen-saturated and heated to 70 °C with moderate stirring under refluxing conditions. Subsequently, 8.6 μL of (3-Aminopropyl)trimethoxysilane (APTMS, Sigma-Aldrich) was added. The NPs dispersion was left under moderate stirring in an inert atmosphere for 6 hours. At the end of the reaction time, the dispersion was collected and centrifuged at 12000 g for 20 minutes. The supernatant was discarded, and the particles were resuspended in 10 mL of ethanol. The process was repeated three times.

2.2. FZ NPs characterization

The crystallinity of the FZ NPs was evaluated through X-ray diffraction (XRD) measurements. Specifically, 1 mg of NPs was deposited onto a monocrystalline silicon wafer and analysed using a Panalytical X'Pert diffractometer operating in Bragg-Brentano mode (Cu Kα source, λ=0.154 nm, 30 mA and 40 kV).

Field Emission Scanning Electron Microscopy (FESEM) was employed to determine morphology and elemental composition of the NPs. Similarly, the FZ NPs were deposited onto a silicon wafer and analysed using a SUPRA 40 microscope from Zeiss equipped with an energy-dispersive X-ray spectroscopy (EDS) detector (Oxford Instruments).

A higher magnification image of the FZ NPs was obtained through Transmission Electron Microscopy (TEM). The FZ NPs were dispersed in water at a concentration of 25 μg/mL, and 10 μL of this solution was deposited on a Lacey carbon support grid (300 mesh, Cu, Ted Pella Inc.). When the solvent was completely evaporated, the grid was analysed using a Talos F200X G2 S(TEM), Thermo Scientific, at an operating voltage of 200 kV.

Finally, the magnetic behaviour of the FZ NPs was investigated in quasistatic conditions at room temperature with a DC magnetometer (Lake Shore 7225, Lake Shore Cryotronics Inc.). Specifically, 1 mg of FZ NPs were encapsulated in 100 μL of Durcupan ACM resin, which was then cured at 60 °C for three days as carried out in other studies [4].

2.3. Lipidic coating of FZ NPs and peptide bioconjugation

To enhance the biocompatibility of FZ NPs, a lipidic coating inspired by RNA-based Covid vaccines was utilized to create a shield on the NPs surface, reducing their toxic effects on cells. Specifically, a procedure developed by Conte et al. Conte et al., [14] was employed, choosing the negatively charged lipidic Formulation 3 C$^-$ (hereafter referred to as 3 C for simplicity) to promote an electrostatic attraction to the positively charged FZ NPs.

The negatively charged phospholipid DOPA (18:1 PA, 1,2-dioleoyl-sn-glycero-3-phosphate (sodium salt, chloroform solution), the neutral phospholipid DOPC (18:1 (Δ9-Cis) PC (DOPC), 1,2-dioleoyl-sn-glycero-3-phosphocholine, chloroform solution) and PEGylated lipids with functional amine and maleimide groups (DSPE-PEG(2000) Amine (1,2-distearoyl-sn-glycero-3-phosphoethanolamine-N-[amino(polyethylene glycol)-2000] (ammonium salt)) and DSPE-PEG(2000) Maleimide (1,2-distearoyl-sn-glycero-3-phosphoethanolamine-N-[maleimide(poly-ethylene glycol)-2000] (ammonium salt)), respectively) were all purchased from Avanti Polar Lipids, Merck. Cholesterol in chloroform solution was bought from Sigma-Merck.

For the preparation of the lipidic formulation, the chloroform solution of lipids, resulting in a molar ratio of 50:10:38.5:1.5 of DOPA: DOPC:Cholesterol:DSPE-PEG(2000)-Amine, was dried in a glass vial under vacuum. The dried lipids were rehydrated using an ethanol:water (40:60) solution to achieve a 3 mg/mL lipids dispersion.

An aliquot of FZ NPs ethanolic stock solution was centrifuged at 14000 g for 10 minutes in a 1.5 mL conical centrifuge tube, and the supernatant was discarded to allow the further formation of the phospholipidic shell. Subsequently, a volume of lipidic solution was added to achieve a Lipids: FZ NPs ratio of 1: 2 in weight. The solution was then sonicated for 3 minutes in an ultrasound bath (59 kHz, Branson 3800 CPXH).

Bidistilled water was then quickly added to reach a final FZ NPs concentration of 1 mg/mL and a final sonication of 5 minutes was performed to obtain the 3 C lipid-coated FZ NPs (FZ-3C NPs).

To incorporate an active targeting mechanism, DSPE-PEG(2000)-Maleimide was conjugated with a YSA peptide (whole aminoacidic sequence YSAYPDSVPMMS [36]) able to specifically bind to EphA2 cell surface receptor and not to other EphA receptors. EphA2 is indeed overexpressed in the osteosarcoma cancer cells used in this study (Figure S3 of SI). To efficiently bioconjugate the peptide to the lipidic shell, a cysteine unit was also specifically added to the original YSA sequence reported in a previous work [36]. The bioconjugation procedure adopted a ratio of lipidic DSPE-PEG(2000)-Maleimide and YSA peptide of 3:1 in molar amount, similarly to what previously reported by some of us [3,5,56]. The lipid was first dried in a glass vial under vacuum and then resuspended in dimethylformamide (DMF, Sigma-Aldrich) at a concentration of 37.5 mM. The peptide was suspended as well in DMF at the concentration of 50 mM. The peptide solution was diluted in 0.1 M of phosphate buffered saline (PBS, pH 7.4) to reach a final concentration of 10 mM of peptide solution.

The lipid solution was added to the mixture to reach a final concentration of 15 mM for the DSPE-PEG(2000)-maleimide and 5 mM of the peptide. After combining the two solutions in the required molar ratio, the mixture was left at room temperature for 1 hour and finally stored at −20 °C. To produce a YSA-bioconjugated 3 C lipidic shell, 0.30 mol% of DSPE-PEG(2000)-YSA was added to the lipidic Formulation 3 C before the drying step. The resulting rehydrated lipidic solution was then used to coat FZ NPs as reported above, and called FZ-3C-YSA NPs.

2.4. Characterization of the lipid-coated NPs

Dynamic light scattering (DLS) was employed to determine the hydrodynamic size of the NPs before and after their shielding with the lipidic coating in both b.d. water and cell culture medium (McCoy 5 A, ATCC, supplemented with 10 % of Fetal Bovine Serum (FBS), ATCC and 1 % of 100 μg/mL of streptomycin, and 100 units/mL of penicillin, Sigma-Aldrich). A solution with a NPs concentration of 100 μg/mL was separately prepared for both media and analysed using a Zetasizer Nano ZS90 (Malvern Panalytical). Similarly, the NPs were evaluated for their Z-potential in b.d. water at neutral pH.

To estimate the coupling efficiency between the 3 C lipids and the FZ NPs, a colocalization study was performed using spinning disk fluorescence optical microscopy (Nikon Ti-E inverted microscope equipped with Spectra X Lumencor multiple solid state light sources, a 100× PlanAPO objective, NA = 1.30, and Andor Zyla sCMOS camera). FZ NPs were stained with ATTO 647-NHS ester (Sigma, 2 μL of a 2 mg/mL solution per 1 mg of FZ NPs), which binds to the amine functionalization of the particles. The dye was directly added to the ethanolic solution and stirred overnight. Afterwards, the nanoparticles were washed through centrifugation and redispersed three times in ethanol before coupling them with the lipids. After the shell was formed on the nanoparticles, it was stained with the lipophilic $DiOC_{18}(3)$ (DiO) dye (5 μL/mg of nanoparticles, incubation at 37°C for 30 minutes) and washed once by centrifugation (5000 g for 10 minutes) and redispersion in water.

A small amount (5 μL of solution) was deposited on a microscope glass slide and analysed through fluorescence microscopy. The NIS software from Nikon was employed to investigate the colocalization of the two entities that constitute the nanoconstruct.

To visualize the FZ-3C NPs, TEM imaging was also carried out on the freshly prepared sample in water at a concentration of 25 μg/mL. Then 10 μL of this solution was deposited on a Lacey carbon support grid (300

mesh, Cu, Ted Pella Inc.), dried at room temperature and analysed using a Talos F200X G2 S(TEM), Thermo Scientific, at an operating voltage of 60 kV.

2.5. Reactive oxygen species generation under US stimulation in water

The ability of FZ NPs to generate reactive oxygen species under US stimulation was assessed using Electron Paramagnetic Resonance (EPR) spectroscopy coupled with the spin-trapping technique across a wide range of US power densities. To conduct the measurements, 2 mL of 200 μg/mL of NPs suspensions in water were prepared for both FZ and FZ-3C NPs for each US condition considered.

To extend the lifetime of the hydroxyl radicals generated during US stimulation, a chemical trap, namely 5,5-dimethyl-L-pyrroline-N-oxide (DMPO, Sigma-Aldrich) was added to the solution to achieve a final concentration of 10 mM. For each sample, 2 mL of FZ NPs dispersion was placed in a 24-well plate (TC-treated, Thermo Fisher). The plate was then positioned on a 2 cm^2 US transducer (Intelect Mobile 2 Ultrasound, Chattanooga, manufactured by DJO France SAS) and coupled with an acoustic water-based gel (Stosswellen Gel, ELvation Medical GmbH). US stimulation was performed at 1 MHz for 1 minute, with power densities varying between 0.2 and 2.0 W/cm^2. After the stimulation, 50 μL of the NPs suspension was withdrawn with a quartz capillary and placed in the sample holder of the EMXNano X-band spectrometer (Bruker, center field 3426 G, 10 scans, 60 s sweep time). The measurements were repeated twice for all the conditions and compared to the outcomes obtained from simple water stimulation. All the data were processed to derive quantitative information by means of the Bruker Xenon software (Bruker).

2.6. Hemocompatibility assay

To determine whether the lipidic coating was able to increase the NPs hemocompatibility, FZ and FZ-3C NPs were tested with a plasma recalcification test [55,64]. Briefly, FZ and FZ-3C NPs were resuspended in a NaCl solution (0.9 % w/v in water) at a concentration of 200 and 100 μg/mL.

For each sample, 75 μL of human citrated plasma (Human Recovered Plasma Pooled- frozen – Na Citrate from ZenBio) was placed in 6 wells of a 96-well plate and pre-heated at 37°C. Then, 75 μL of sample was added to the wells to obtain final concentrations of 100 and 50 μg/mL. After 5 minutes of 37°C incubation, 150 μL of 25 mM $CaCl_2$ was added into 3 of the 6 wells prepared for each sample. The absorbance at 405 nm was measured with a plate reader (Multiskan GO microplate spectrophotometer, Thermo Fisher Scientific) over time (every 30 seconds over 45 minutes) to assess the coagulation of plasma. The plate was always kept at 37 °C. The coagulation time was determined in three independent experiments following the procedure reported in another work [12].

2.7. 2D cytotoxicity and internalization of FZ, FZ-3C NPs

The cytocompatibility of FZ and FZ-3C NPs was initially assessed in vitro using two osteosarcoma cell lines: MG-63 (ATCC) and SaOS-2 (ATCC). Both cell lines were cultured in McCoy 5 A medium (ATCC), supplemented with 10 % of FBS (ATCC) and 1 % of 100 μg/mL of streptomycin/100 units/mL of penicillin (Sigma-Aldrich), at a temperature of 37°C and 5 % of CO_2.

For cytotoxicity tests, cells were seeded in 96-well plates (TC Treated, Thermo Fisher) at a concentration of 1000 cells/well in 100 μL of cell culture medium to form a cell monolayer. After 24 hours, half of the medium was replaced with medium containing NPs. The NPs were previously added to fresh medium to obtain a concentration twice as the desired one. The final analysed NPs concentrations were 10, 20, 30 and 50 μg/mL. At 24 and 48 h after NPs administration, cell viability was measured using a metabolic colorimetric assay. Specifically, 10 μL of WST-1 reagent (Roche) was added to each well 2 hours before the end of the incubation time. The plate was incubated at 37 °C for 2 hours and the absorbance at 450 nm and 620 nm (the latter used as a refence) was measured with a plate reader (Multiskan GO microplate spectrophotometer, Thermo Fisher Scientific). The measured signal, opportunely background-subtracted, was compared to the one of non-treated cells (set as 100 % cell viability).

Flow cytometry was employed to determine the ability of cells to internalize the synthetized NPs. Considering the importance of the targeting peptide for cell internalization, FZ-3C-YSA NPs were also analysed. For this test, $3{\cdot}10^4$ cells were seeded into a 6-well plate (TC-treated, Cellstar, Greiner) along with 2 mL of cell culture medium. Before NPs administration, NPs were stained with ATTO 647-NHS ester as previously described.

The NPs (FZ, FZ-3C and FZ-3C-YSA) were incubated with the seeded cells at concentrations of 10 and 20 μg/mL (the ones at which the cells remain viable). After 24 and 48 hours, cells were washed twice with PBS (Sigma Aldrich) to remove any non-internalized NPs. Cells were then detached by trypsinization, and the cell suspension was washed twice with PBS by centrifugation and redispersion (130 g for 5 minutes) to obtain a final volume of 300 μL. The cell suspension was analysed by means of a Guava easyCyte 6–2 L flow cytometer (Merck Millipore), following a standard procedure already described elsewhere [51]. The analysis of the results was conducted with the InCyte software (Merck Millipore).

All the biological tests described above and those that follow were carried out at least in triplicates, and ANOVA tests were performed with the software SigmaPlot 14.0. Two ways or three ways ANOVA tests were performed according to the number of parameters considered in the experiment. p-values lower than 0.05 were considered statistically significant.

2.8. 3D cytotoxicity of FZ and FZ-3C

The NPs cytotoxicity was also assessed on 3D spheroids of bone osteosarcoma using the MG-63 cell line. The decision to use only the MG-63 cell line was due to the difficulty in obtaining optimal 3D spheroids with SaOS-2 cells.

To prepare MG-63 cells spheroids, $1.5{\cdot}10^4$ cells/well were seeded in an ultra-low attachment (ULA) round-bottom 96-well plate (Corning) with 100 μL of the same culture medium used for 2D cultures. The entire plate was centrifuged at 250 g for 5 minutes to facilitate the settling of cells at the bottom of the well. Cells were allowed to grow for one week and were monitored through bright-field microscopy to observe and confirm the spheroid formation. The spheroid diameters were measured twice for each spheroid along perpendicular axes.

For the cytotoxicity test, spheroids were gently extracted with 50 μL of their original medium using a micropipette and transferred to a suspension cell culture flat-bottom 96-well plate (Greiner Bio-One). After that, 50 μL of a double-concentrated NPs suspension, similarly to the protocol used in monolayer cell cultures, was added to each well to achieve final concentrations of 10, 20, 30 and 50 μg/mL. The WST-1 assay was once again employed to determine the cell viability. More in detail, 10 μL of WST-1 solution was added to each well and the incubation time for the spheroids was extended to 3 hours to enhance the signal-over-noise ratio. After the incubation period, i.e., at 24 and 48 hours from NP administration, the absorbance of the solution was measured with the same procedure applied for 2D cell cultures.

A qualitative estimation of cytotoxicity was also performed by means of confocal microscopy, as further described in the following sections.

2.9. NP-assisted US stimulation on 3D spheroids with FZ, FZ-3C and FZ-3C-YSA NPs

The effectiveness of NP-assisted US stimulation on cells subjected to NPs administration was evaluated for 3D osteosarcoma spheroids. The

decision to directly proceed with a more complex system was based on the way US propagates within the well. As demonstrated in the work by Tamboia et al. Tamboia et al., [63], the section of the well closer to the bottom is less sensitive to US radiation compared to the whole volume in which the cells are cultured. A single cell monolayer might not be directly exposed to the US radiation as a 3D structure. As a proof of concept, to better simulate potential in vivo scenarios involving complex 3D structures, sonodynamic therapy was directly applied to MG-63 cell line spheroids.

For these tests, after 7 days of spheroids growth in ULA plates, 4 spheroids in 50 μL each were transferred with a micropipette to a well of an untreated 24-well plate (Corning). Cell culture medium containing NPs was added to each well to obtain a final concentration of 20 μg/mL. The NPs used included FZ, FZ-3C and FZ-3C-YSA NPs. After 24 h from NPs administration, the wells were stimulated with US at power densities of 1.0 and 2.0 W/cm^2 for 1 minute. Immediately after sonostimulation, the spheroids were separated and placed in the well of a 96-well plate together with 100 μL of cell culture medium. After 24 h, cell viability was assessed by the WST-1 assay, similarly to the method employed for cell cytotoxicity evaluation.

2.10. Fluorescence microscopy

The spinning disk fluorescence microscope mentioned above was employed for confocal microscopy analysis of MG-63 spheroids.

Initially, a qualitative study on NPs cytotoxicity was conducted. Spheroids were cultured following the same procedure used for the metabolic viability assay and placed in a 96-well flat-bottom plate (Greiner Bio-One). For each analysed timepoint (24 and 48 h), the following dyes were added to the cell culture medium: Calcein-AM dye (ThermoFisher, 1 μL/mL of final medium solution) to label viable cells, Hoechst 33342 dye (ThermoFisher, 0.6 μL/mL) to label cell nuclei, and Propidium Iodine (PI, ThermoFisher, 2 μL/mL), which is cell impermeable and binds to DNA, allowing for dead cells labelling. A total of 50 μL of dye-containing medium (three times concentrated)) was added to the spheroids (already suspended in a 100 μL volume). After 3 hours of incubation at 37°C, the spheroids were analysed by fluorescence microscopy.

A similar procedure was used to assess the spheroids' viability after sonostimulation. In the case of internalization studies, cells were labelled with Wheat Germ Agglutin 488 (WGA-488, 2.4 μL/mL of the final medium), Hoechst 33342 (ThermoFisher, 0.6 μL/mL), and Propidium Iodine (ThermoFisher, 2 μL/mL). Additionally, ATTO 647-labelled NPs were used to perform spheroid internalization tests under fluorescence microscopy. The spheroids were placed on chamber slides (Nunc Lab-Tek II CC2 Chamber Slide system, Thermo Fisher Scientific) to enable image capture at a higher magnification and incubated with ATTO 647-labelled FZ, FZ-3C and FZ-3C-YSA.

3. Results and discussion

3.1. FZ NPs chemical and physical characterization

Before their exploitation in biological systems, FZ NPs were analysed

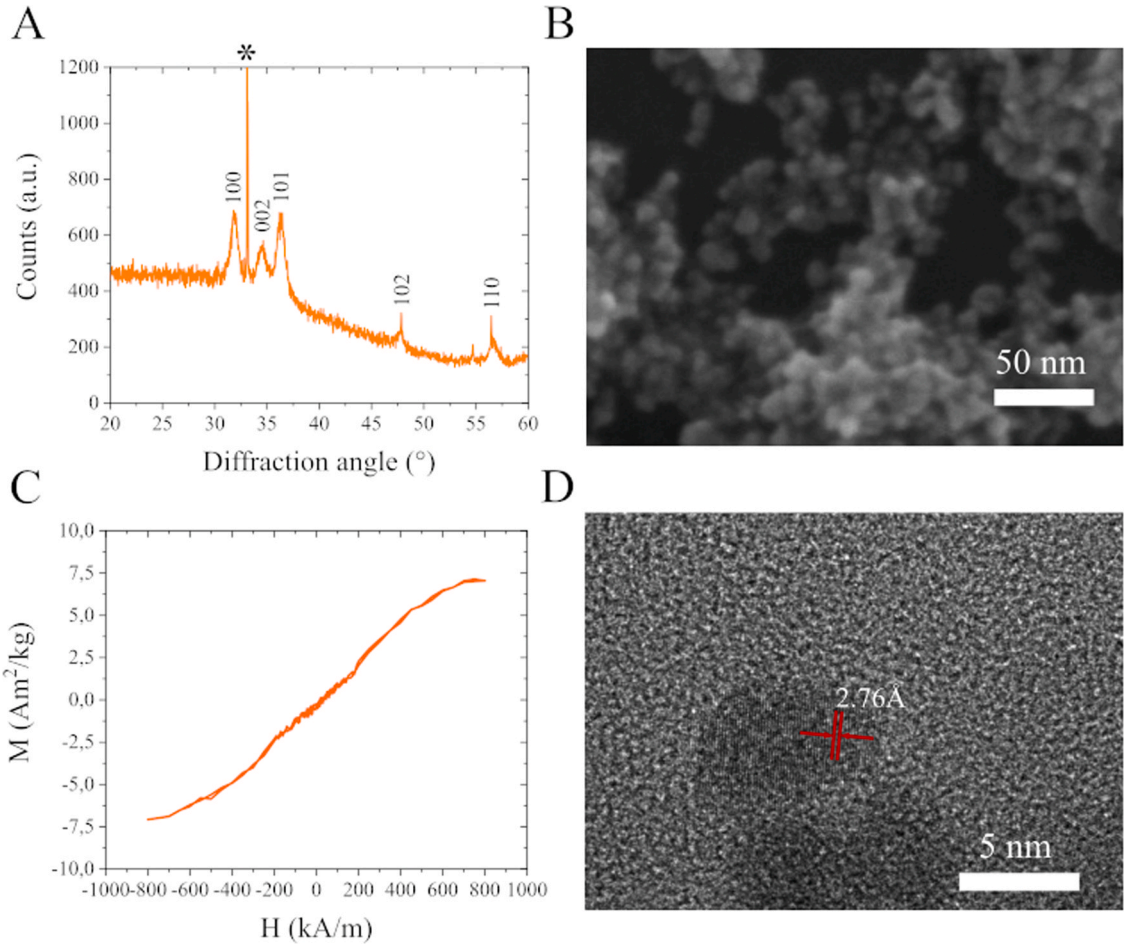

Fig. 1. Characterization of the FZ NPs. A) XRD pattern (the number over the peaks correspond to the Miller indices of the crystalline planes, while the * mark denotes the peak belonging to the silicon substrate onto which the nanoparticles were deposited prior their measurement), B) representative FESEM image, C) saturation-magnetization curve showing the magnetic properties of the FZ NPs and D) representative high resolution TEM image.

in terms of crystallinity, morphology, and magnetic properties. The XRD pattern (Fig. 1A) reports diffraction peaks which can all be assigned to the wurtzitic crystalline structure of FZ NPs (see the Miller indexes to which each plane is assigned, according to JCPDS-ICDD, card No. 89-1397). The very sharp and intense peak around 33° is in contrast attributed to the monocrystalline silicon substrate. No additional diffraction peaks can be recognized, indicating that only ZnO was obtained, and that the iron doping atoms are not clustering nor forming separate crystalline phase inside the particles.

The NPs morphology was determined by means of electron microscopy. As it can be noticed from Fig. 1B, FZ NPs have a spherical morphology and possess a diameter that ranges between 4 and 8 nm. The EDS analysis indicates that the ratio between Fe and Zn atoms is 5.05 % (1.19 for Fe at% and 23.67 Zn at%). This value is remarkably similar to the amount of precursor included during the synthesis (6 % of atomic ratio). Oxygen is also present with 75.10 at%. The absence of stoichiometry between Zn and O can be attributed to the native silicon oxide layer on top of the silicon wafer and the oleic acid capping. In this

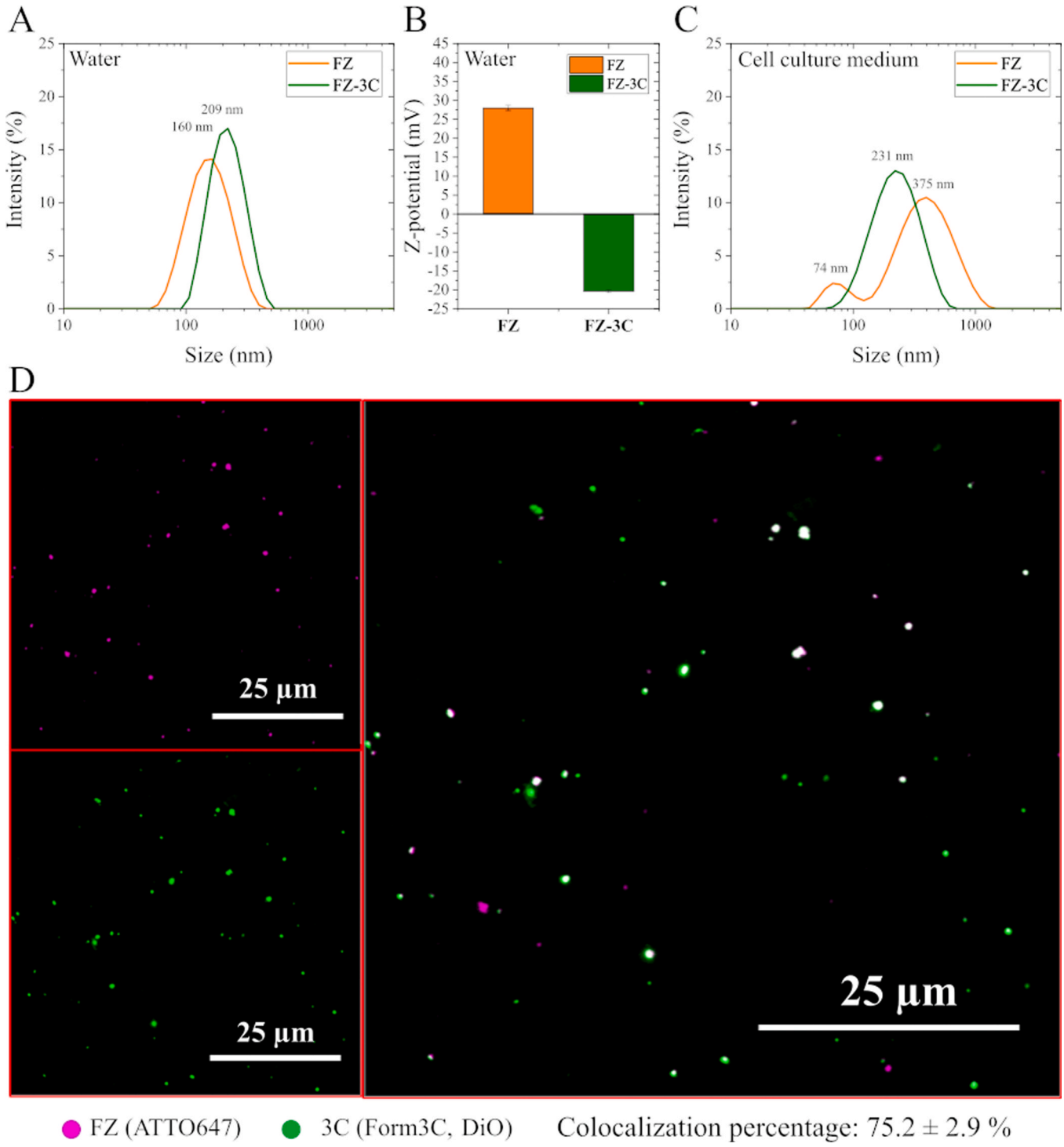

Fig. 2. Characterization of the FZ NPs coated with lipids. DLS measurements of FZ (orange curve) and FZ-3C NPs (green curve) in A) b.d. water and C) McCoy 5 A cell culture medium supplemented with 10 % of FBS. B) Z-potential measurements belongs to the NPs in water prior and after their coating with lipids. D) Confocal microscopy images of the FZ-3C NPs. The FZ NPs are labelled with ATTO 647 (purple), the lipidic coating with the DiO dye (green).

analysis silicon contribution was excluded by the percentage computation because it belongs to the substrate.

The high resolution TEM measurement reported in Fig. 1D confirms the results found by XRD and FESEM analyses. Indeed, the lattice spacing measured in the TEM image (2.746 ± 0.03 Å) is very close to the one obtained by the XRD pattern (2.811 Å) for the 100 plane. Additionally, it is possible to observe that FZ NPs present a single crystalline domain in their boundaries, indicating a substantial monocrystalline habit of each nanoparticle.

Recently, iron doping has been proposed to induce magnetic properties in ZnO materials, conferring potentialities in terms of magnetic resonance imaging [11,18] or magnetic particle imaging [75,79]. Fig. 1C reports the magnetic behaviour of the synthetized FZ NPs. As it can be seen from the saturation-magnetization curve, the FZ NPs present a paramagnetic behaviour with a magnetization saturation at 7.5 Am^2/kg.

3.2. FZ-3C NPs characterization

FZ NPs were subsequently coated with a lipidic shell aimed to increase their biocompatibility and their stability in biological media. To assess the success of the coating and the increase of biostability, DLS measurements were performed and the results compared among FZ NPs and lipid coated FZ-3C NPs. As it can be seen in Fig. 2A, both the pristine FZ NPs (orange curve) and the lipid-coated FZ-3C NPs (green curve) in water show monodisperse behaviour, with a relatively sharp distribution peaking at 160 nm for FZ NPs and 208 nm for FZ-3C NPs.

Concerning the hydrodynamic diameter of FZ NPs, when compared to the dimension found in the electron microscopy images in Fig. 1, this measurement results larger than expected. This is due to a certain degree of aggregation of the particles in water which tend to form small clusters. Still, their dispersibility in water is good (PDI = 0.135), indicating that the clusters are mono-distributed in size.

When the lipidic shell coats the NPs, the hydrodynamic diameter is increased up to 208 nm, probably due to the increase of the diameter of the overall nanoconstruct. The dispersibility is also very good with a PDI of 0.115. It is fair to suppose that the lipidic shell does not cover a single NP but a cluster of them, resulting in a nanostructure that has an overall diameter of approximately 200 nm. A further confirmation of this finding is provided by TEM analysis (reported in Fig. S1 of the Supporting Information, S.I.), where it is possible to observe the coating of the lipidic shell on top of FZ NPs small aggregates.

When immersed in FBS-supplemented cell culture medium (Fig. 2C), the pristine FZ NPs present a very different DLS profile, with two size distribution peaks, at 74 nm and at 375 nm. The PDI is larger, with a value equal to 0.313, than the one measured in water. This may indicate aggregation and a partial dissolution of the NPs, which are known to degrade in biological media [19]. The behaviour of the lipid-coated particles is in contrast unchanged with respect to that obtained in water. Indeed, the diameter is 231 nm (against the 209 nm in water) and the PDI = 0.141. Clearly, the phospholipidic shell is a boost for the good dispersibility and stability of the particles in biological media, which are fundamental aspects for their hemocompatibility, cytotoxicity and optimal nanometric size. This result is in accordance with a previous work in which a similar method was used and the stability over time of the nanoconstruct was demonstrated for one entire week [14].

The success of the coating is also corroborated by the change in the Z-potential of the particles (Fig. 2B). Indeed, FZ NPs have a marked positive Z-potential (+28 mV) that guarantees their stability in water (but not in cell culture medium). When coated with the phospholipidic shell, the Z-potential is reduced up to a negative value (-20.4 mV) which assures again their biostability while also preventing the interaction between particles and biological medium. The strong negative potential of the particles clearly suggests that their surface is coated with a negative moiety which is very likely to be the negative phospholipidic formulation.

To quantify the effectiveness of the coating, a colocalization study employing the

fluorescence microscope was performed. In this test, the particles were labelled with a dye (ATTO 647) that produces a far-red emission upon red light exposure. The lipidic coating was stained with a lipophilic dye that emits in the green region of light (DiO). The images of the particles were collected and analysed and, a quantitative estimation of the FZ NPs coupled with 3 C lipids was obtained by means of a colocalization routine developed by Nikon in the NIS software. Indeed, the colocalization of the two fluorescent signals on the same spot indicates that the two moieties coexist in the same space, allowing to suppose the coating of the NPs by the lipid. A representative example is reported in Fig. 2D, where most of the spots are colocalized. The quantitative estimation of all acquired colocalization images has an average of 75.2 ± 2.9 % of the total NPs.

3.3. Reactive oxygen species generation under US stimulation in water

There is a considerable body of literature regarding the generation of ROS upon ZnO micro and nanomaterials exposure to US radiation [33,44,65,67]. They can be successfully exploited in cancer therapy since an excessive presence of intracellular ROS may be effective in cancer cell killing [1,17]. This work aims to activate safe-by-design ZnO NPs by means of a harmless US radiation to specifically induce cancer cell death only in the desired site. Therefore, we measured the ROS generation of lipid-coated and uncoated FZ NPs in water when exposed to US irradiation by means of EPR spectroscopy and compared it to the one generated by water alone under US irradiation [8]. More in detail, the measurements were performed to determine the generation and the concentration of hydroxyl radicals, which are very specific to the DMPO chemical trap and already observed to be the most abundant contribution in radical formation during ZnO NPs solutions or water exposure to US [2,32,48,74].

As it can be clearly noticed in Fig. 3, the signature of the spin adducts of DMPO-OH are clearly visible in all samples at US power densities above 0.4 W/cm^2. In particular, when the pristine FZ NPs are irradiated by US, ROS are generated in a larger amount with respect to the simple water solution. Interestingly, the introduction of the phospholipidic coating reduces the amount of generated ROS. This could be potentially attributed to a scavenging effect of the organic lipidic shell. Indeed, organic molecules are well known to react with ROS [2] and probably, thanks to the close proximity of the lipids to the ZnO surface, they are favoured to react with the ROS with respect to the chemical trap. Still, ROS are generated also with coated FZ-3C and, at the highest US power density, the ROS amount is very similar to the one generated by water alone. In view of the in vitro and future in vivo applications of the NPs, it is clear that some other mechanisms should be included i to improve their efficacy. It is thus hypothesized that, if the lipidic coating is able to increase the bio and hemocompatibility of the NPs, a larger dose of nanoparticles could therefore be safely administered, increasing the efficacy of the treatment as well. Furthermore, the targeting provided by the YSA peptide to a selected cell type, i.e. the cancer one, is expected to further increase the internalization of the NPs and selectively drive the cytotoxic ROS production to the cancerous tissue only. These assumptions will be verified in the following.

3.4. Hemocompatibility assay

Another important aspect that must be considered when designing a therapeutic or diagnostic moiety is the ability to be safely injected in the body. Therefore, the hemocompatibility of FZ and FZ-3C NPs was evaluated with a plasma clotting assay.

Indeed, the time interval that plasma takes to clot when in contact with either FZ NPs or the coated FZ-3C NPs was measured. As it can be noticed in Fig. 4, the plasma clotting time (calculated from UV-Vis absorbance measurements reported in Fig. S2 of Supporting

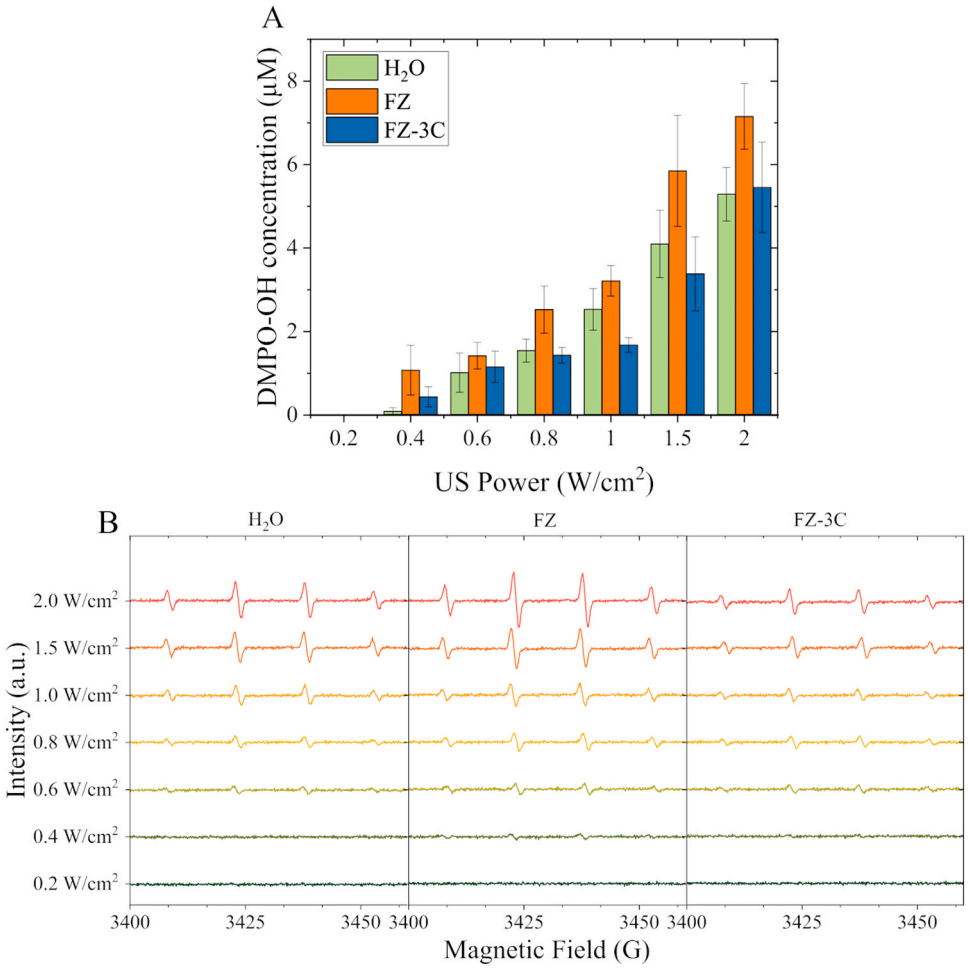

Fig. 3. A) Reactive oxygen species generation in water under US stimulation quantification. B) Spin adducts of the fabricated NPs at different US power densities.

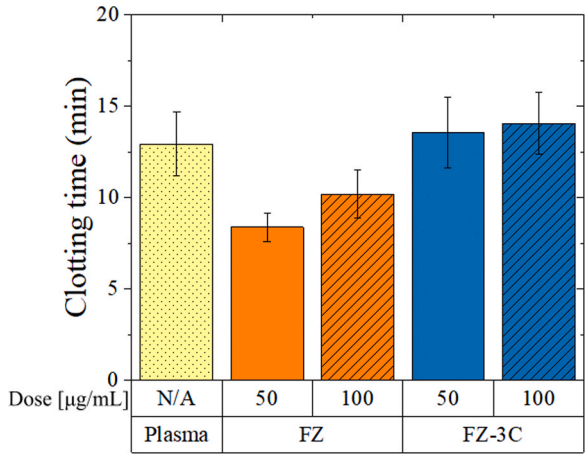

Fig. 4. Hemocompatibility studies of FZ and FZ-3C NPs comparing the times required for the plasma to coagulate in presence of both the NPs.

Information, S.I.) in the presence of calcium chloride is of approximately 13 minutes. This time is reduced to 8.4 and 10.2 minutes for naked FZ NPs at 50 and 100 μg/mL, respectively. When the coated nanoparticles are considered, it is possible to observe a substantial increase of the clotting time with respect to the naked NPs. The obtained values are 13.6 and 14.1 minutes for 50 and 100 μg/mL respectively, which is very close to the one of reference plasma. This result underlines the importance of providing a lipidic coating to the NPs even if this might affect the efficacy of ROS generation under US treatment. Indeed, even if the pristine FZ nanoparticles are physically more effective in generating ROS, an in vivo exploitation of these nanoparticles is limited because of the high probability of blood clots formation in the patient. Also, the lipidic coating is effective in reducing the cytotoxicity of the NPs themselves, as demonstrated below and already proved in the work of Conte et al. Conte et al., [14], allowing the potential exploitation of larger doses of coated NPs in cells than the pristine one.

3.5. FZ and FZ-3C cytotoxicity and internalization studies on MG-63 and SaOS-2 osteosarcoma cell lines as 2D monolayer

FZ and FZ-3C were tested on two osteosarcoma cell lines to determine the effectiveness of the lipidic coating in increasing the highest NPs safe dose that can be administered without triggering any cytotoxic effect. This is required since the system is envisioned to induce a cytotoxic effect only when activated by a US radiation. The cytotoxicity results obtained with a metabolic assay for MG-63 and SaOS-2 cell lines are reported in Figs. 5A and 5B respectively. As it can be observed from the graph, FZ NPs start to become cytotoxic at doses higher than 20 μg/mL for both cell lines. When the nanoparticles are coated with the Formulation 3 C, cell viability exceeds 80 % for all the considered doses, indicating the low toxicity of the nanoconstructs up to 50 μg/mL. A statistically significant difference in viability between FZ and FZ-3C NPs can be found for all the doses from 20 μg/mL to 50 μg/mL, for both cell lines (see the complete analysis reported in the S.I.), confirming the effectiveness of the lipid coating regardless the cell line considered. The

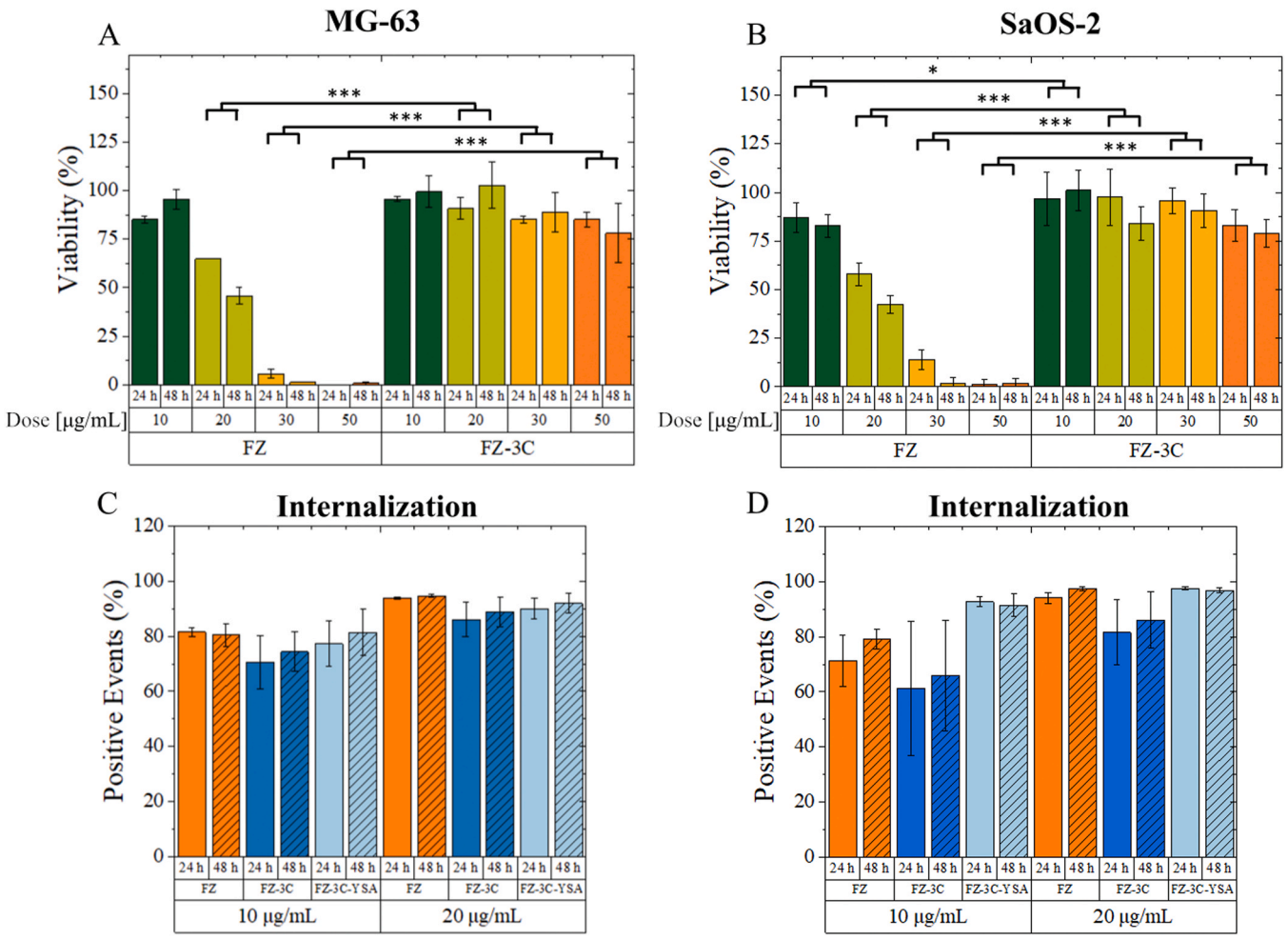

Fig. 5. Cytotoxicity of FZ and FZ-Form-3C NPs on the A) MG-63 and B) SaOS-2 cell lines in monolayer cell culture, confirming the increase in biocompatibility of the FZ-3C when compared to the FZ- NPs. Internalization of FZ and FZ-Form-3C NPs in the C) MG-63 and D) SaOS-2 cell lines in monolayer cell culture analyzed by flow cytometry. Data are reported as percentage of positive events, intended as the percentage of cells having a fluorescence signal higher than the one of the control cells and therefore that have internalized at least a fluorescently-labelled NP. Three ways ANOVA was performed on the data. For graph readability, only relevant statistically significant differences are shown (***$p < 0.001$, **$p < 0.01$, and *$p < 0.05$), for a complete report on the statistics refer to Supporting Information.

use of iron doping, previously shown to enhance the safety profile of pure ZnO NPs [11,26,76], coupled with their encapsulation in a lipidic coating, has been demonstrated to generally enhance the biosafety of the FZ NPs. This is further supported by their demonstrated safety in non-cancerous cell lines in prior studies [14,68].

Cellscapability to internalize the proposed NPs was also investigated by flow cytometry (Figs. 5C and 5D). The role of the YSA peptide, targeting the EphA2 protein overexpressed in these tumor cell lines was also investigated. In particular, the Western Blot analysis shows a higher expression of EphA2 in the SaOS-2 cell line than in MG-63 cells (see Figure S3 in the S.I.).

The results of flow cytometry analyses show that the internalization of pristine FZ NPs approaches 80 % of positive events for the MG-63 cell lines already at 10 μg/mL dose. The percentage of positive events is raised to 90 % with the increase of the dose to 20 μg/mL. The high internalization of the bare FZ NPs may be due to their positive surface charge that generates an electrostatic attraction toward the negative cell membrane [53]. When NPs are coated with a lipidic coating (FZ-3C), a reduction of the positive events percentages is observed. This is expected since the Z-potential of the nanoparticles is negative and therefore the electrostatic attraction is reduced. This is why the addition of a targeting peptide becomes essential. Indeed, when the targeting peptide is bioconjugated to the lipid shell, the positive events increase again in average, showing excellent internalization capabilities of the FZ-3C-YSA in both cell lines and compensating for the negative Z-potential of the NPs. This phenomenon is even enhanced with the SaOS-2 cell line in which the FZ-3C-YSA NPs present a higher percentage of positive events than FZ NPs at 10 μg/mL and a statistically significant (full analysis in S. I.) difference between FZ-3C and FZ-3C-YSA NPs.

The difference between the FZ-3C NPs with and without targeting peptide can be appreciated in both cell lines. The higher level of NP internalization in cells as well as the peptide-mediated internalization process are all factors that can contribute to influence the behaviour of NPs inside the cells, leading to a possible higher killing capability of the nanoconstructs when activated by the US radiation.

3.6. Cytotoxicity and internalization of NPs on 3D spheroids of MG-63 cells

FZ and FZ-3C NPs were finally tested on 3D spheroids of cells belonging to the MG-63 cell line. A first metabolic evaluation of the NPs cytotoxicity was performed. Fig. 6A highlights a trend that is similar to the one found for the 2D cell cultures. The viability of cell spheroids is already below 70 % for the lowest considered dose (10 μg/mL) of pristine FZ NPs. The viability decreases with the increase of NPs dose, reaching a value close to 30 % for 30 μg/mL and almost 0 % at the highest dose considered (50 μg/mL). In contrast, the spheroid viability with the coated FZ-3C NPs is generally higher and oscillates between

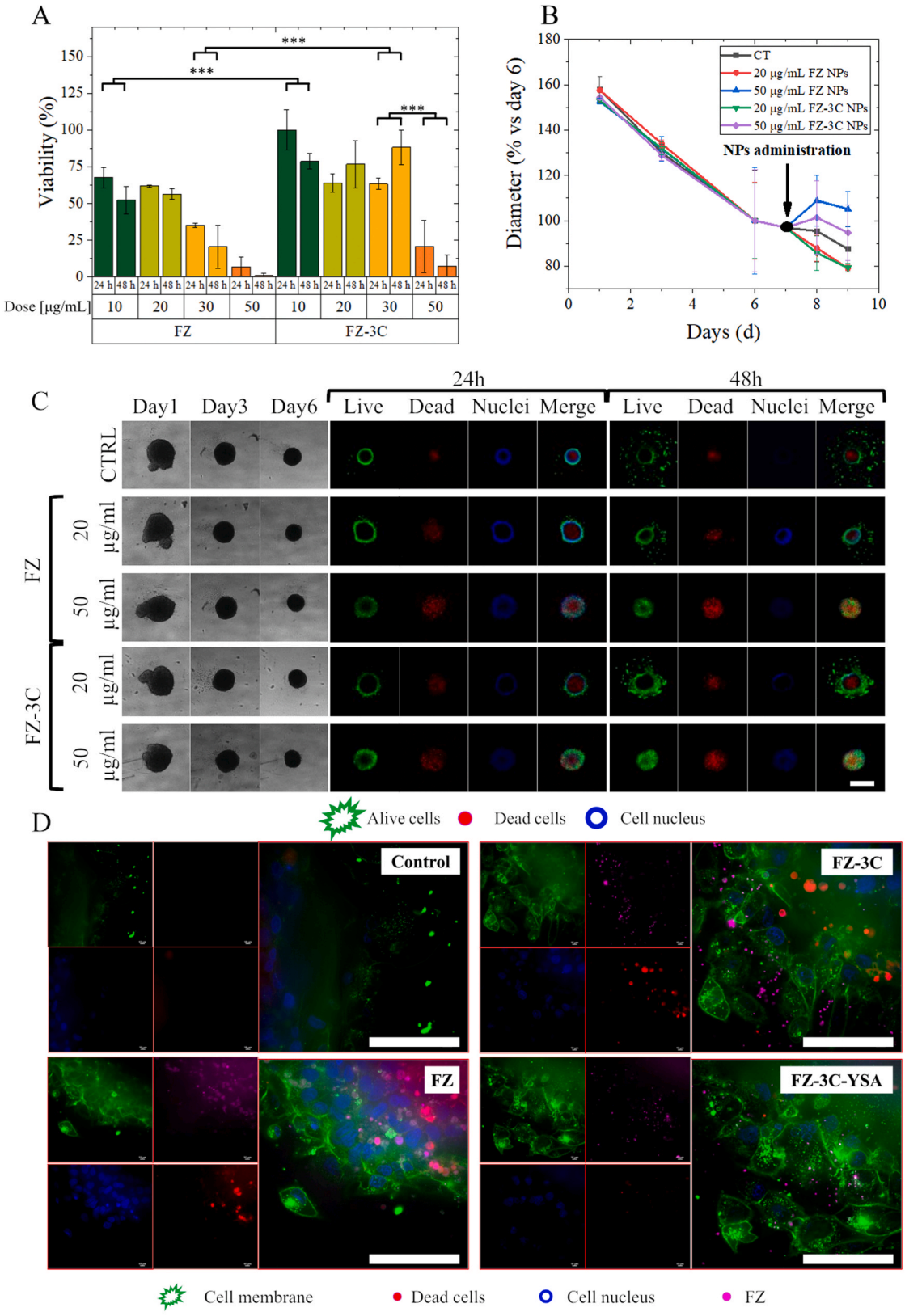

Fig. 6. A) Cytotoxicity of FZ and FZ-3C NPs in 3D MG-63 cell line spheroids. B) Evolution of the mean spheroid diameter over 10 days (NPs administered on day 7). On the 7th day, the diameter was calculated as the mean between the diameter at day 6 and the one at day 8. Three ways ANOVA was performed on the data. For graph readability, only relevant statistically significant differences are shown (***$p < 0.001$, **$p < 0.01$, and *$p < 0.05$), for a complete report on the statistics refer to Supporting Information. C) Confocal fluorescence microscopy of 3D MG-63 cell line spheroids. Calcein is exploited to label live cells (green), PI (red) to identify dead cells and Hoechst (blue) to label cells nuclei. Scalebar is 500 μm. Confocal fluorescence microscopy of 3D MG-63 cell line spheroids. WGA is exploited to label live cells (green), ATTO 647-NHS ester (purple) to identify the nanoparticles (FZ, FZ-3C and FZ-3C-YSA) and Hoechst (blue) to label cells nuclei. Scalebar is 100 μm.

75 % and 100 % for the concentrations ranging from 10 to 30 μg/mL. Interestingly, at 50 μg/mL there is a significant toxicity with the coated NPs as well, not observed with the 2D cell culture, suggesting a higher sensibility of the spheroid when compared to the 2D monolayers and further evidencing the need for a 3D model to assess the behaviour of the NPs. As shown in Fig. S4 of the S.I., the introduction of the targeting peptide is not affecting cell viability.

Another interesting aspect rises from the microscopy evaluation of the diameter of the spheroids. In Fig. 6B the diameters of the spheroids are reported as percentage of the diameter measured at day 6 (the day before spheroid treatment): it is possible to observe a consistent reduction over time of all the spheroid diameters since the first day up to the 6th day (prior to NPs treatment). This behaviour clearly persists up to the 10th day for both the control spheroids (black curve) and those treated with safe concentrations of NPs (see the red and green curves in Fig. 6B). However, according to the literature, the spheroid size is not always a reliable indicator of cell viability [7]. Thus, it cannot be concluded that a reduction in spheroid diameter always indicates a decrease in viability. Indeed, when cultured in 3D fashion, cells develop an outer zone containing proliferating cells, while the internal ones goes toward necrosis [62], probably consolidating and compacting the cells, with a consequent reduction of the spheroid dimension. Still, the spheroid size can provide useful information on the behaviour of cells when subjected to a treatment. Indeed, starting from the day after the NPs administration (day 7), it is possible to observe an abrupt increase of the diameter in the spheroids treated with toxic doses of NPs, i.e. FZ and FZ-3C at 50 μg/mL (blue and violet lines, respectively). It is hypothesized that the reduced spheroid metabolism is due to the presence of excessive amount of zinc cations coming from the dissolution of the ZnO NPs, well reported in the literature to be cytotoxic and able to disrupt cells' zinc homeostasis [9], possibly leading to morphological changes in the spheroids.

An optical estimation of the spheroid condition was also performed by means of fluorescence microscopy. The control spheroid in the first raw of Fig. 6C shows a decrease of the diameter over the first 6 days and a further reduction over the next days. Despite the clear viability of the outer cell layer of the spheroid, the inner core presents a red signal that is related to cell death. This agrees to what is typically found in the literature. Indeed, the core of the spheroid is not easily reached by the nutrients, resulting in its quiescence or even necrosis [7]. Interestingly, as the spheroid is moved from the ultra-low attachment to the flat bottom 96-well plate, it starts to spread on the well bottom with a visible proliferation of adherent cells after 48 h from its transfer. This confirms the high viability of the outer cell layer that is firstly indicated by the calcein green signal. As for what concerns the NPs-treated spheroids, for FZ and FZ-3C at 20 μg/mL, the green fluorescent signal is well visible after 24 and 48 h from the NPs administration showing a good spheroid viability and the spread of some cells at the bottom of the well. In contrast, at cytotoxic doses of both FZ and FZ-3C (i.e. 50 μg/mL) the red signal, related to cell death, increases with time. Interestingly, when the spheroids are completely dead, they are not disrupted.

An investigation of the NPs internalization was performed also in the case of the spheroids. Unfortunately, it was not possible to perform flow cytometry analysis with spheroids because the process required for cell disruption with trypsin was not effective, probably due to the strong tightening that cells show during the spheroid's formation and the possible calcification of this specific type of spheroids. Therefore, a fluorescence microscopy analysis was conducted at the edges of the spheroids and some representative images are reported in Fig. 6D. It is possible to observe a diffuse purple signal representing the ATTO 647 dye associated to the NPs inside all the spheroids treated with the pristine FZ NPs. These results suggest a high level of pristine NPs internalization and a broad distribution inside the spheroid, in comparison with the control spheroid, in which the purple signal related to the NPs is reasonably absent. These data confirm the findings already obtained in the 2D flow cytometry. In the specific case of FZ-3C NPs, it is possible to observe some NPs outside the cells, and the absence of a strong diffuse signal inside the spheroid. A higher signal is in contrast found with the targeting peptide for the FZ-3C-YSA NPs, suggesting a higher level of internalization with respect to the lipidic coated FZ-3C ones, as already highlighted in the 2D internalization assay.

3.7. NP-assisted US stimulation on MG-63 spheroids

As demonstrated by the above results, the proposed lipid-coated NPs are meant to be safe by design until stimulated with a remote activation, i.e. acoustic pressure stimulation of US, which triggers a cytotoxic response in the biological system. The EPR measurements highlighted the scavenging effect of lipids toward hydroxyl radicals production, therefore an active targeting mechanism was developed to enhance the internalization of the NPs and, as a consequence, their intracellular accumulation and ROS generation upon US stimulation. Indeed, the most cytotoxic response in the spheroids is obtained when applying the NPs coated with peptide-functionalized lipidic shell and the US irradiation at the highest power density. More in details, in Fig. 7A, the metabolic activity of MG-63 spheroids is evaluated after the different nanoconstructs' administration and their stimulation with US 24 hours later. The evaluation was performed at two power densities, i.e. at 1 and 2 W/cm^2, for 1 minute.

The selection of the US dose, in terms of frequency used, power density and application time, was driven by the safety concept: the US irradiation, in the absence of NPs, should not be toxic for the spheroids, as visible by the green bars of Fig. 7A. The spheroids show a reduced (70 %) cell viability at the highest applied power (2 W/cm^2) which is not statistically different from the control. At the intermediate US power density (1 W/cm^2) the viability is close to 80 %. Interestingly, the administration of the NPs and the US impairs the spheroid cell viability at a different extent depending on the used NPs. As expected, the pristine FZ NPs are very toxic when coupled with the US radiation, echoing our previous works [51,52] even if the toxicity of FZ-NPs themselves prevents statistically significant differences among the various US treatments. This can be simply attributed to the higher level of ROS generated in presence of the NPs. A less pronounced toxicity is observed with the lipid coated FZ-3C NPs, despite a statistically significant difference can be found between FZ-3C NPs without US stimulation and the one with 2 W/cm^2. This result agrees with that obtained by the EPR measurements, where a scavenging of the produced ROS by the lipidic shell was hypothesized. Still, mechanical damages due to the NPs are possible, in a similar way to what already observed in the case of mechanical stimulations with shock waves, providing the so-called "nanoscalpel effect" [10] even in the absence of ROS.

As mentioned above, the most important result is obtained when applying the NPs coated with peptide-functionalized lipidic shell and the US irradiation to the spheroids. Indeed, the mean value of their metabolic activity is even lower than the one obtained with the pristine NPs for the 1 W/cm^2 power density, with a statistically significant difference in viability of the sample without US stimulation with 1 and 2 W/cm^2 samples. The reason of this behaviour could be attributed to a higher level of internalization that the targeting peptide provides with respect to the other NPs, increasing their intracellular level.

Another interesting aspect of the results in Fig. 7A is that, at the highest power density considered (2 W/cm^2), there is almost no more difference among the type of NPs employed. Presumably, the mechanical damage triggered by the NPs coupled with the US stimulation becomes predominant with respect to the ROS generation.

Finally, Fig. 7B qualitatively shows the effect of the NPs coupled with the US stimulation on the spheroids. Despite clear differences are very difficult to spot because vital cells are always present in all the considered samples, it is still possible to appreciate small discrepancies among them. First of all, the spheroids stimulated with a power density of 2 W/cm^2 present very similar features, with the red signal related to dead cells that pervades the whole volume of the spheroid. In the case of 1 W/

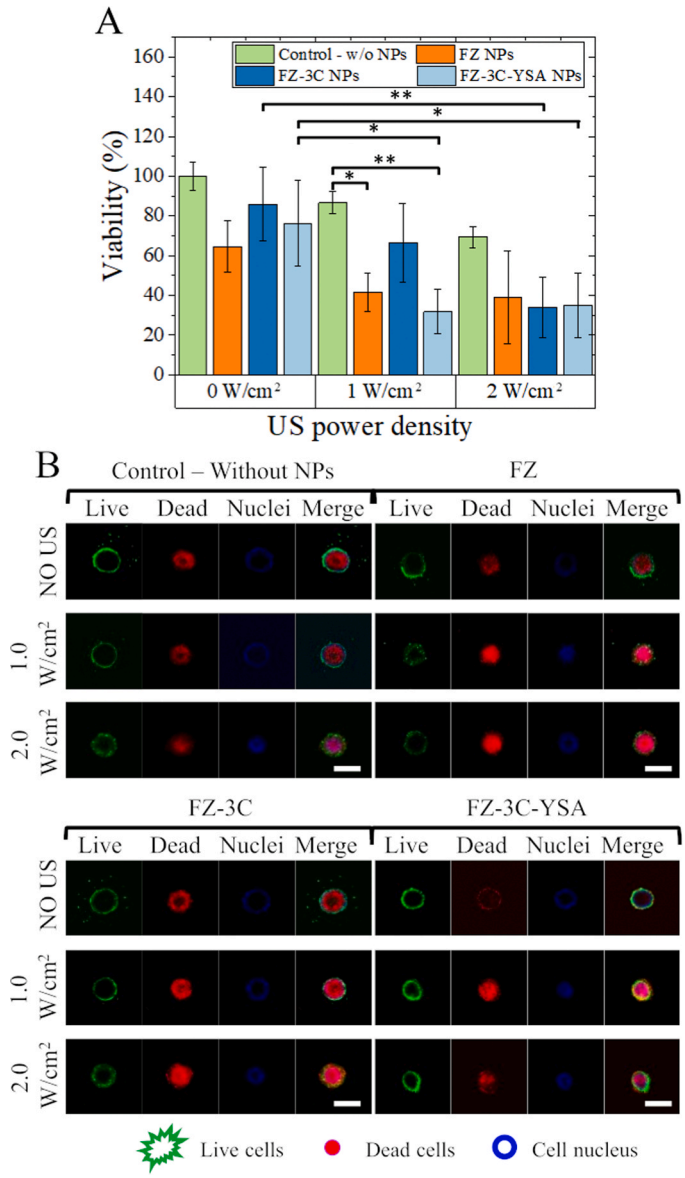

Fig. 7. A) Viability evaluation based on the metabolic activity of MG-63 spheroids after the administration of FZ, FZ-3C and FZ-3C-YSA and the NP-assisted US stimulation. Two ways ANOVA was performed on the data. For graph readability, only relevant statistically significant differences are shown (***$p < 0.001$, **$p < 0.01$, and *$p < 0.05$), for a complete report on the statistics refer to Supporting Information. B) Effect of the NP-assisted US stimulation on MG-63 spheroids after the administration of FZ, FZ-3C and FZ-3C-YSA. The analysis was performed with a confocal microscopy. Scalebar is 500 μm.

cm^2 US stimulation, the spheroids treated with FZ-3C NPs present a red signal in the spheroid core and a well-defined viable cells perimeter. In the case of FZ and FZ-3C-YSA NPs, the red-labelled dead cells are present in the whole volume of the spheroid. Although qualitative, these results indicate that FZ NPs and FZ-3C-YSA NPs cause severe cell damage when coupled with the US stimulation. Interestingly, the use of the targeting peptide increases considerably its efficacy by restoring the cytotoxic effect of the pristine FZ nanoconstruct, while preserving the very high efficiency of the lipidic coating in enhancing the biocompatibility, biostability and hemocompatibility of the NPs, as reported above.

4. Conclusions

Iron-doped ZnO NPs coated with a peptide-targeted phospholipidic layer, coupled with ultrasound irradiation are proposed as potential therapeutic agents for the treatment of osteosarcoma. The underlying concept of this work is to fabricate a biomimetic nanoconstruct that is safe-by-design and targeted to trigger a specific cytotoxic action towards cancer cells only when remotely activated by a mechanical pressure stimulation. The NPs activation with US allows the generation of ROS and potentially other mechanical damages, in a sufficient amount to be effective in killing cancer cells. Efficient cancer cell killing by the targeted nanoconstruct for sonodynamic therapy was proven in both 2D cell monolayers and in 3D cell spheroid models paving the way for new nanomedicine and remotely-triggered and stimuli-responsive tools for osteosarcoma treatment. Future directions entail the validation of the nanoconstruct within increasingly complex 3D cell cultures, more closely mirroring in vivo conditions, thereby facilitating the effective implementation of the integrated NPs-SD therapy.

CRediT authorship contribution statement

Marco Carofiglio: Writing – original draft, Visualization, Methodology, Investigation, Data curation, Conceptualization. **Giulia Mesiano:** Writing – review & editing, Methodology, Data curation, Conceptualization. **Giada Rosso:** Writing – review & editing, Investigation, Data curation. **Marzia Conte:** Writing – review & editing, Investigation, Data curation. **Marco Zuccheri:** Investigation, Data curation. **Ymera Pignochino:** Writing – review & editing, Methodology. **Valentina Cauda:** Writing – review & editing, Supervision, Resources, Project administration, Funding acquisition, Conceptualization.

Declaration of Competing Interest

The authors declare the following financial interests/personal relationships which may be considered as potential competing interests: Valentina Cauda reports financial support was provided by European Innovation Council. Valentina Cauda reports financial support was provided by Italian Ministry of University and Research. Ymera Pignochino reports financial support was provided by Italian Ministry of Health. The other authors declare that they have no known competing financial interests nor personal relationships that could have appeared to influence the work reported in this paper.

Data availability

Data will be made available on request.

Acknowledgements

This project has received funding from the European Union's Horizon 2020 research and innovation program under grant agreement No. 964386_project acronym "MimicKEY". The project has also received funding from the Italian PRIN project of the Ministero dell'Università e della Ricerca 2020MHL8S9 "MITHOS" and from Italian Ministry of Health (GR2016-02362726).

Appendix A. Supporting information

Supplementary data associated with this article can be found in the online version at doi:10.1016/j.mtcomm.2024.109826.

References

[1] P. Agostinis, K. Berg, K.A. Cengel, T.H. Foster, A.W. Girotti, S.O. Gollnick, S. M. Hahn, M.R. Hamblin, A. Juzeniene, D. Kessel, M. Korbelik, J. Moan, P. Mroz, D. Nowis, J. Piette, B.C. Wilson, J. Golab, Photodynamic therapy of cancer: an

update, CA: A Cancer J. Clin. 61 (2011) 250–281, https://doi.org/10.3322/caac.20114.
[2] A. Ancona, A. Troia, N. Garino, B. Dumontel, V. Cauda, G. Canavese, Leveraging rechargeable nanobubbles on amine-functionalized ZnO nanocrystals for sustained ultrasound cavitation towards echographic imaging, Ultrason. Sonochem. 67 (2020) 105132, https://doi.org/10.1016/j.ultsonch.2020.105132.
[3] S. Barui, M. Conte, N.M. Percivalle, R.M.G. Montero, L. Racca, M. Allione, V. Cauda, Dual drug loaded nanotheranostic platforms as a novel synergistic approach to improve pancreatic cancer treatment, Part. Part. Syst. Charact. 40 (2023) 2200138, https://doi.org/10.1002/ppsc.202200138.
[4] S. Barui, R. Gerbaldo, N. Garino, R. Brescia, F. Laviano, V. Cauda, Facile chemical synthesis of doped ZnO nanocrystals exploiting oleic acid, Nanomaterials 10 (2020) 1150, https://doi.org/10.3390/nano10061150.
[5] S. Barui, N.M. Percivalle, M. Conte, B. Dumontel, L. Racca, M. Carofiglio, V. Cauda, Development of doped ZnO-based biomimicking and tumor targeted nanotheranostics to improve pancreatic cancer treatment, Cancer Nanotechnol. (2022).
[6] C. Brazzale, R. Canaparo, L. Racca, F. Foglietta, G. Durando, R. Fantozzi, P. Caliceti, S. Salmaso, L. Serpe, Enhanced selective sonosensitizing efficacy of ultrasound-based anticancer treatment by targeted gold nanoparticles, Nanomedicine 11 (2016) 3053–3070, https://doi.org/10.2217/nnm-2016-0293.
[7] S.C. Brüningk, I. Rivens, C. Box, U. Oelfke, G. ter Haar, 3D tumour spheroids for the prediction of the effects of radiation and hyperthermia treatments, Sci. Rep. 10 (2020) 1653, https://doi.org/10.1038/s41598-020-58569-4.
[8] G. Canavese, A. Ancona, L. Racca, M. Canta, B. Dumontel, F. Barbaresco, T. Limongi, V. Cauda, Nanoparticle-assisted ultrasound: a special focus on sonodynamic therapy against cancer, Chem. Eng. J., Smart Nanomater. Nanostruct. Diagn. Ther. 340 (2018) 155–172, https://doi.org/10.1016/j.cej.2018.01.060.
[9] M. Canta, V. Cauda, The investigation of the parameters affecting the ZnO nanoparticle cytotoxicity behaviour: a tutorial review, Biomater. Sci. 8 (2020) 6157–6174, https://doi.org/10.1039/D0BM01086C.
[10] M. Carofiglio, M. Conte, L. Racca, V. Cauda, Synergistic phenomena between iron-doped ZnO nanoparticles and shock waves exploited against pancreatic cancer cells, ACS Appl. Nano Mater. (2022), https://doi.org/10.1021/acsanm.2c04211.
[11] M. Carofiglio, M. Laurenti, V. Vighetto, L. Racca, S. Barui, N. Garino, R. Gerbaldo, F. Laviano, V. Cauda, Iron-doped ZnO nanoparticles as multifunctional nanoplatforms for theranostics, Nanomaterials 11 (2021) 2628, https://doi.org/10.3390/nano11102628.
[12] V. Cauda, T.T. Xu, I. Nunes, E. Mereu, S. Villata, E. Bergaggio, M. Labrador, T. Limongi, F. Susa, A. Chiodoni, M. Cumerlato, G. Rosso, R. Stefania, R. Piva, Biomimetic mesoporous vectors enabling the efficient inhibition of wild-type isocitrate dehydrogenase in multiple myeloma cells, Microporous Mesoporous Mater. 325 (2021) 111320, https://doi.org/10.1016/j.micromeso.2021.111320.
[13] G. Chiabotto, G. Grignani, M. Todorovic, V. Martin, M.L. Centomo, E. Prola, G. Giordano, A. Merlini, U. Miglio, E. Berrino, L. Napione, C. Isella, F. Capozzi, M. Basiricò, C. Marsero, I. Gerardi, T. Venesio, D. Sangiolo, M. Aglietta, L. D'Ambrosio, Y. Pignochino, Pazopanib and trametinib as a synergistic strategy against osteosarcoma: preclinical activity and molecular insights, Cancers 12 (2020) 1519, https://doi.org/10.3390/cancers12061519.
[14] M. Conte, M. Carofiglio, G. Rosso, V. Cauda, Lipidic formulations inspired by COVID vaccines as smart coatings to enhance nanoparticle-based cancer therapy, Nanomaterials 13 (2023) 2250, https://doi.org/10.3390/nano13152250.
[15] X. Dai, Y. Shao, X. Tian, X. Cao, L. Ye, P. Gao, H. Cheng, X. Wang, Fusion between glioma stem cells and mesenchymal stem cells promotes malignant progression in 3D-bioprinted models, ACS Appl. Mater. Interfaces 14 (2022) 35344–35356, https://doi.org/10.1021/acsami.2c06658.
[16] C. Deng, M. Zheng, S. Han, Y. Wang, J. Xin, O. Aras, L. Cheng, F. An, GSH-activated porphyrin sonosensitizer prodrug for fluorescence imaging-guided cancer sonodynamic therapy, Adv. Funct. Mater. 33 (2023) 2300348, https://doi.org/10.1002/adfm.202300348.
[17] D.E.J.G.J. Dolmans, D. Fukumura, R.K. Jain, Photodynamic therapy for cancer, Nat. Rev. Cancer 3 (2003) 380–387, https://doi.org/10.1038/nrc1071.
[18] H. Du, F. Yang, C. Yao, Z. Zhong, P. Jiang, S.G. Stanciu, H. Peng, J. Hu, B. Jiang, Z. Li, W. Lv, F. Zheng, H.A. Stenmark, A. Wu, Multifunctional modulation of high-performance ZnxFe3−xO4 nanoparticles by precisely tuning the zinc doping content, Small 18 (2022) 2201669, https://doi.org/10.1002/smll.202201669.
[19] B. Dumontel, M. Canta, H. Engelke, A. Chiodoni, L. Racca, A. Ancona, T. Limongi, G. Canavese, V. Cauda, Enhanced biostability and cellular uptake of zinc oxide nanocrystals shielded with a phospholipid bilayer, J. Mater. Chem. B 5 (2017) 8799–8813, https://doi.org/10.1039/C7TB02229H.
[20] B. Dumontel, F. Susa, T. Limongi, M. Canta, L. Racca, A. Chiodoni, N. Garino, G. Chiabotto, M.L. Centomo, Y. Pignochino, V. Cauda, ZnO nanocrystals shuttled by extracellular vesicles as effective Trojan nano-horses against cancer cells, Nanomedicine 14 (2019) 2815–2833, https://doi.org/10.2217/nnm-2019-0231.
[21] B. Dumontel, F. Susa, T. Limongi, V. Vighetto, D. Debellis, M. Canta, V. Cauda, Nanotechnological engineering of extracellular vesicles for the development of actively targeted hybrid nanodevices, Cell Biosci. 12 (2022) 61, https://doi.org/10.1186/s13578-022-00784-9.
[22] EMA implements new measures to minimise animal testing during medicines development | European Medicines Agency [WWW Document], n.d. URL ⟨https://www.ema.europa.eu/en/news/ema-implements-new-measures-minimise-animal-testing-during-medicines-development⟩ (accessed 5.21.24).
[23] P. Fathi, L. Rao, X. Chen, Extracellular vesicle-coated nanoparticles, VIEW 2 (2021) 20200187, https://doi.org/10.1002/VIW.20200187.
[24] F. Foglietta, L. Serpe, R. Canaparo, The effective combination between 3D cancer models and stimuli-responsive nanoscale drug delivery systems, Cells 10 (2021) 3295, https://doi.org/10.3390/cells10123295.
[25] F. Gao, G. He, H. Yin, J. Chen, Y. Liu, C. Lan, S. Zhang, B. Yang, Titania-coated 2D gold nanoplates as nanoagents for synergistic photothermal/sonodynamic therapy in the second near-infrared window, Nanoscale 11 (2019) 2374–2384, https://doi.org/10.1039/C8NR07188H.
[26] S. George, S. Pokhrel, T. Xia, B. Gilbert, Z. Ji, M. Schowalter, A. Rosenauer, R. Damoiseaux, K.A. Bradley, L. Mädler, A.E. Nel, Use of a rapid cytotoxicity screening approach to engineer a safer zinc oxide nanoparticle through iron doping, ACS Nano 4 (2010) 15–29, https://doi.org/10.1021/nn901503q.
[27] G. Giordano, A. Merlini, G. Ferrero, G. Mesiano, E. Fiorino, S. Brusco, M. L. Centomo, V. Leuci, L. D'Ambrosio, M. Aglietta, D. Sangiolo, G. Grignani, Y. Pignochino, EphA2 expression in bone sarcomas: bioinformatic analyses and preclinical characterization in patient-derived models of osteosarcoma, ewing's sarcoma and chondrosarcoma, Cells 10 (2021) 2893, https://doi.org/10.3390/cells10112893.
[28] W. Guo, T. Wang, C. Huang, S. Ning, Q. Guo, W. Zhang, H. Yang, D. Zhu, Q. Huang, H. Qian, X. Wang, Platelet membrane-coated C-TiO2 hollow nanospheres for combined sonodynamic and alkyl-radical cancer therapy, Nano Res 16 (2023) 782–791, https://doi.org/10.1007/s12274-022-4646-2.
[29] X. Han, J. Huang, X. Jing, D. Yang, H. Lin, Z. Wang, P. Li, Y. Chen, Oxygen-deficient black titania for synergistic/enhanced sonodynamic and photoinduced cancer therapy at near infrared-II biowindow, ACS Nano 12 (2018) 4545–4555, https://doi.org/10.1021/acsnano.8b00899.
[30] Z. Hu, X. Song, L. Ding, Y. Cai, L. Yu, L. Zhang, Y. Zhou, Y. Chen, Engineering Fe/Mn-doped zinc oxide nanosonosensitizers for ultrasound-activated and multiple ferroptosis-augmented nanodynamic tumor suppression, Mater. Today Bio 16 (2022) 100452, https://doi.org/10.1016/j.mtbio.2022.100452.
[31] B. Illes, P. Hirschle, S. Barnert, V. Cauda, S. Wuttke, H. Engelke, Exosome-coated metal–organic framework nanoparticles: an efficient drug delivery platform, Chem. Mater. 29 (2017) 8042–8046, https://doi.org/10.1021/acs.chemmater.7b02358.
[32] N.H. Ince, G. Tezcanli, R.K. Belen, İ.G. Apikyan, Ultrasound as a catalyzer of aqueous reaction systems: the state of the art and environmental applications, Appl. Catal. B: Environ. 29 (2001) 167–176, https://doi.org/10.1016/S0926-3373(00)00224-1.
[33] K.P. Jyothi, S. Yesodharan, E.P. Yesodharan, Ultrasound (US), Ultraviolet light (UV) and combination (US+UV) assisted semiconductor catalysed degradation of organic pollutants in water: oscillation in the concentration of hydrogen peroxide formed in situ, Ultrason. Sonochem. 21 (2014) 1787–1796, https://doi.org/10.1016/j.ultsonch.2014.03.019.
[34] A. Kheirolomoom, L.M. Mahakian, C.-Y. Lai, H.A. Lindfors, J.W. Seo, E.E. Paoli, K. D. Watson, E.M. Haynam, E.S. Ingham, L. Xing, R.H. Cheng, A.D. Borowsky, R. D. Cardiff, K.W. Ferrara, Copper−doxorubicin as a nanoparticle cargo retains efficacy with minimal toxicity, Mol. Pharm. 7 (2010) 1948–1958, https://doi.org/10.1021/mp100245u.
[35] B. Kip, C.U. Tunc, O. Aydin, Triple-combination therapy assisted with ultrasound-active gold nanoparticles and ultrasound therapy against 3D cisplatin-resistant ovarian cancer model, Ultrason. Sonochem. 82 (2022) 105903, https://doi.org/10.1016/j.ultsonch.2021.105903.
[36] M. Koolpe, M. Dail, E.B. Pasquale, An ephrin mimetic peptide that selectively targets the EphA2 receptor, J. Biol. Chem. 277 (2002) 46974–46979, https://doi.org/10.1074/jbc.M208495200.
[37] R. Leenhardt, M. Camus, J.L. Mestas, M. Jeljeli, E. Abou Ali, S. Chouzenoux, B. Bordacahar, C. Nicco, F. Batteux, C. Lafon, F. Prat, Ultrasound-induced Cavitation enhances the efficacy of chemotherapy in a 3D model of pancreatic ductal adenocarcinoma with its microenvironment, Sci. Rep. 9 (2019) 18916, https://doi.org/10.1038/s41598-019-55388-0.
[38] I. Lentacker, I. De Cock, R. Deckers, S.C. De Smedt, C.T.W. Moonen, Understanding ultrasound induced sonoporation: definitions and underlying mechanisms, Adv. Drug Deliv. Rev., Ultrasound triggered Drug Deliv. 72 (2014) 49–64, https://doi.org/10.1016/j.addr.2013.11.008.
[39] Y. Li, L. Hao, F. Liu, L. Yin, S. Yan, H. Zhao, X. Ding, Y. Guo, Y. Cao, P. Li, Z. Wang, H. Ran, Y. Sun, Cell penetrating peptide-modified nanoparticles for tumor targeted imaging and synergistic effect of sonodynamic/HIFU therapy, Int. J. Nanomed. 14 (2019) 5875–5894, https://doi.org/10.2147/IJN.S212184.
[40] Y. Li, Q. Zhou, Z. Deng, M. Pan, X. Liu, J. Wu, F. Yan, H. Zheng, IR-780 dye as a sonosensitizer for sonodynamic therapy of breast tumor, Sci. Rep. 6 (2016) 25968, https://doi.org/10.1038/srep25968.
[41] X. Lin, J. Song, X. Chen, H. Yang, Ultrasound-activated sensitizers and applications, Angew. Chem. Int. Ed. 59 (2020) 14212–14233, https://doi.org/10.1002/anie.201906823.
[42] P. Liu, G. Chen, J. Zhang, A review of liposomes as a drug delivery system: current status of approved products, regulatory environments, and future perspectives, Molecules 27 (2022) 1372, https://doi.org/10.3390/molecules27041372.
[43] Y. Liu, Ying Wang, W. Zhen, Yinghui Wang, S. Zhang, Y. Zhao, S. Song, Z. Wu, H. Zhang, Defect modified zinc oxide with augmenting sonodynamic reactive oxygen species generation, Biomaterials 251 (2020) 120075, https://doi.org/10.1016/j.biomaterials.2020.120075.
[44] C. Lops, A. Ancona, K. Di Cesare, B. Dumontel, N. Garino, G. Canavese, S. Hérnandez, V. Cauda, Sonophotocatalytic degradation mechanisms of rhodamine B dye via radicals generation by micro- and nano-particles of ZnO, Appl. Catal. B: Environ. 243 (2019) 629–640, https://doi.org/10.1016/j.apcatb.2018.10.078.

[45] M.W. Miller, D.L. Miller, A.A. Brayman, A review of in vitro bioeffects of inertial ultrasonic cavitation from a mechanistic perspective, Ultrasound Med. Biol. 22 (1996) 1131–1154, https://doi.org/10.1016/S0301-5629(96)00089-0.
[46] L. Mirabello, R.J. Troisi, S.A. Savage, International osteosarcoma incidence patterns in children and adolescents, middle ages, and elderly persons. Int J. Cancer 125 (2009) 229–234, https://doi.org/10.1002/ijc.24320.
[47] L. Mirabello, R.J. Troisi, S.A. Savage, Osteosarcoma incidence and survival rates from 1973 to 2004: data from the surveillance, epidemiology, and end results program, Cancer 115 (2009) 1531–1543, https://doi.org/10.1002/cncr.24121.
[48] V. Mišík, P. Riesz, Free radical intermediates in sonodynamic therapy, Ann. N. Y. Acad. Sci. 899 (2000) 335–348, https://doi.org/10.1111/j.1749-6632.2000.tb06198.x.
[49] L.A. Osminkina, A.L. Nikolaev, A.P. Sviridov, N.V. Andronova, K.P. Tamarov, M. B. Gongalsky, A.A. Kudryavtsev, H.M. Treshalina, V.Yu Timoshenko, Porous silicon nanoparticles as efficient sensitizers for sonodynamic therapy of cancer, Microporous Mesoporous Mater. 210 (2015) 169–175, https://doi.org/10.1016/j.micromeso.2015.02.037.
[50] X. Qian, Y. Zheng, Y. Chen, Micro/nanoparticle-augmented sonodynamic therapy (SDT): breaking the depth shallow of photoactivation, Adv. Mater. 28 (2016) 8097–8129, https://doi.org/10.1002/adma.201602012.
[51] L. Racca, T. Limongi, V. Vighetto, B. Dumontel, A. Ancona, M. Canta, G. Canavese, N. Garino, V. Cauda, Zinc oxide nanocrystals and high-energy shock waves: a new synergy for the treatment of cancer cells, Front. Bioeng. Biotechnol. 8 (2020), https://doi.org/10.3389/fbioe.2020.00577.
[52] L. Racca, G. Rosso, M. Carofiglio, S. Fagoonee, G. Mesiano, F. Altruda, V. Cauda, Effective combination of biocompatible zinc oxide nanocrystals and high-energy shock waves for the treatment of colorectal cancer, Cancer Nanotechnol. 14 (2023) 37, https://doi.org/10.1186/s12645-023-00195-6.
[53] A.A. Ramahi, R.L. Ruff, Membrane Potential, in: M.J. Aminoff, R.B. Daroff (Eds.), Encyclopedia of the Neurological Sciences (Second Edition), Academic Press, Oxford, 2014, pp. 1034–1035, https://doi.org/10.1016/B978-0-12-385157-4.00062-2.
[54] M. Sancho-Albero, M. del M. Encabo-Berzosa, M. Beltrán-Visiedo, L. Fernández-Messina, V. Sebastián, F. Sánchez-Madrid, M. Arruebo, J. Santamaría, P. Martín-Duque, Efficient encapsulation of theranostic nanoparticles in cell-derived exosomes: leveraging the exosomal biogenesis pathway to obtain hollow gold nanoparticle-hybrids, Nanoscale 11 (2019) 18825–18836, https://doi.org/10.1039/C9NR06183E.
[55] C. Santos, S. Turiel, P. Sousa Gomes, E. Costa, A. Santos-Silva, P. Quadros, J. Duarte, S. Battistuzzo, M.H. Fernandes, Vascular biosafety of commercial hydroxyapatite particles: discrepancy between blood compatibility assays and endothelial cell behavior, J. Nanobiotechnol. 16 (2018) 27, https://doi.org/10.1186/s12951-018-0357-y.
[56] M.R. Schnorenberg, S.P. Yoo, M.V. Tirrell, J.L. LaBelle, Synthesis and purification of homogeneous lipid-based peptide nanocarriers by overcoming phospholipid ester hydrolysis, ACS Omega 3 (2018) 14144–14150, https://doi.org/10.1021/acsomega.8b01772.
[57] A. Schroeder, R. Honen, K. Turjeman, A. Gabizon, J. Kost, Y. Barenholz, Ultrasound triggered release of cisplatin from liposomes in murine tumors, J. Control. Release 137 (2009) 63–68, https://doi.org/10.1016/j.jconrel.2009.03.007.
[58] P.C. Searson, The Cancer Moonshot, the role of in vitro models, model accuracy, and the need for validation, Nat. Nanotechnol. 18 (2023) 1121–1123, https://doi.org/10.1038/s41565-023-01486-0.
[59] A. Sirelkhatim, S. Mahmud, A. Seeni, N.H.M. Kaus, L.C. Ann, S.K.M. Bakhori, H. Hasan, D. Mohamad, Review on zinc oxide nanoparticles: antibacterial activity and toxicity mechanism, Nano-Micro Lett. 7 (2015) 219–242, https://doi.org/10.1007/s40820-015-0040-x.
[60] S. Stolik, J.A. Delgado, A. Pérez, L. Anasagasti, Measurement of the penetration depths of red and near infrared light in human “ex vivo” tissues, J. Photochem. Photobiol. B: Biol. 57 (2000) 90–93, https://doi.org/10.1016/S1011-1344(00)00082-8.
[61] K.S. Suslick, Sonochemistry, Science 247 (1990) 1439–1445, https://doi.org/10.1126/science.247.4949.1439.
[62] R.M. Sutherland, J.A. McCredie, W.R. Inch, Growth of Multicell Spheroids in Tissue Culture as a Model of Nodular Carcinomas2, JNCI: J. Natl. Cancer Inst. 46 (1971) 113–120, https://doi.org/10.1093/jnci/46.1.113.
[63] G. Tamboia, M. Campanini, V. Vighetto, L. Racca, L. Spigarelli, G. Canavese, V. Cauda, A comparative analysis of low intensity ultrasound effects on living cells: from simulation to experiments, Biomed. Micro 24 (2022) 35, https://doi.org/10.1007/s10544-022-00635-x.
[64] R. Tavano, D. Segat, E. Reddi, J. Kos, M. Rojnik, P. Kocbek, S. Iratni, D. Scheglmann, M. Colucci, I.M.R. Echevarria, F. Selvestrel, F. Mancin, E. Papini, Procoagulant properties of bare and highly PEGylated vinyl-modified silica nanoparticles, Nanomedicine 5 (2010) 881–896, https://doi.org/10.2217/nnm.10.65.
[65] Q. Truong Hoang, V. Ravichandran, T.G. Nguyen Cao, J.H. Kang, Y.T. Ko, T.I. Lee, M.S. Shim, Piezoelectric Au-decorated ZnO nanorods: ultrasound-triggered generation of ROS for piezocatalytic cancer therapy, Chem. Eng. J. 435 (2022) 135039, https://doi.org/10.1016/j.cej.2022.135039.
[66] F. Vakhshiteh, Z. Bagheri, M. Soleimani, A. Ahvaraki, P. Pournemat, S.E. Alavi, Z. Madjd, Heterotypic tumor spheroids: a platform for nanomedicine evaluation, J. Nanobiotechnology 21 (2023) 249, https://doi.org/10.1186/s12951-023-02021-y.
[67] V. Vighetto, A. Ancona, L. Racca, T. Limongi, A. Troia, G. Canavese, V. Cauda, The Synergistic effect of nanocrystals combined with ultrasound in the generation of reactive oxygen species for biomedical applications, Front. Bioeng. Biotechnol. 7 (2019) 374, https://doi.org/10.3389/fbioe.2019.00374.
[68] V. Vighetto, M. Conte, G. Rosso, M. Carofiglio, F. Sidoti Abate, L. Racca, G. Mesiano, V. Cauda, Anti-CD38 targeted nanotrojan horses stimulated by acoustic waves as therapeutic nanotools selectively against Burkitt’s lymphoma cells, Discov. Nano 19 (2024) 28, https://doi.org/10.1186/s11671-024-03976-z.
[69] V. Vighetto, L. Racca, M. Canta, J.C. Matos, B. Dumontel, M.C. Gonçalves, V. Cauda, Smart shockwave responsive titania-based nanoparticles for cancer treatment, Pharmaceutics 13 (2021) 1423, https://doi.org/10.3390/pharmaceutics13091423.
[70] F. Wang, B. Wang, W. You, G. Chen, Y.-Z. You, Integrating Au and ZnO nanoparticles onto graphene nanosheet for enhanced sonodynamic therapy, Nano Res (2022), https://doi.org/10.1007/s12274-022-4599-5.
[71] X. Wang, X. Zhong, L. Bai, J. Xu, F. Gong, Z. Dong, Z. Yang, Z. Zeng, Z. Liu, L. Cheng, Ultrafine titanium monoxide (TiO1+x) nanorods for enhanced sonodynamic therapy, J. Am. Chem. Soc. 142 (2020) 6527–6537, https://doi.org/10.1021/jacs.9b10228.
[72] X. Wang, X. Zhong, F. Gong, Y. Chao, L. Cheng, Newly developed strategies for improving sonodynamic therapy, Mater. Horiz. 7 (2020) 2028–2046, https://doi.org/10.1039/D0MH00613K.
[73] Xianwen Wang, Xiyu Wang, Q. Yue, H. Xu, X. Zhong, L. Sun, G. Li, Y. Gong, N. Yang, Z. Wang, Z. Liu, L. Cheng, Liquid exfoliation of TiN nanodots as novel sonosensitizers for photothermal-enhanced sonodynamic therapy against cancer, Nano Today 39 (2021) 101170, https://doi.org/10.1016/j.nantod.2021.101170.
[74] L.K. Weavers, F.H. Ling, M.R. Hoffmann, Aromatic compound degradation in water using a combination of sonolysis and ozonolysis, Environ. Sci. Technol. 32 (1998) 2727–2733, https://doi.org/10.1021/es970675a.
[75] J. Weizenecker, B. Gleich, J. Rahmer, H. Dahnke, J. Borgert, Three-dimensional real-time in vivo magnetic particle imaging, Phys. Med. Biol. 54 (2009) L1, https://doi.org/10.1088/0031-9155/54/5/L01.
[76] T. Xia, Y. Zhao, T. Sager, S. George, S. Pokhrel, N. Li, D. Schoenfeld, H. Meng, Sijie Lin, X. Wang, M. Wang, Z. Ji, J.I. Zink, L. Mädler, V. Castranova, Shuo Lin, A. E. Nel, Decreased dissolution of ZnO by iron doping yields nanoparticles with reduced toxicity in the rodent lung and zebrafish embryos, ACS Nano 5 (2011) 1223–1235, https://doi.org/10.1021/nn1028482.
[77] Y. Yang, X. Wang, H. Qian, L. Cheng, Titanium-based sonosensitizers for sonodynamic cancer therapy, Appl. Mater. Today 25 (2021) 101215, https://doi.org/10.1016/j.apmt.2021.101215.
[78] T. Yong, Xiaoqiong Zhang, N. Bie, H. Zhang, Xuting Zhang, F. Li, A. Hakeem, J. Hu, L. Gan, H.A. Santos, X. Yang, Tumor exosome-based nanoparticles are efficient drug carriers for chemotherapy, Nat. Commun. 10 (2019) 3838, https://doi.org/10.1038/s41467-019-11718-4.
[79] E.Y. Yu, M. Bishop, B. Zheng, R.M. Ferguson, A.P. Khandhar, S.J. Kemp, K. M. Krishnan, P.W. Goodwill, S.M. Conolly, Magnetic particle imaging: a novel in vivo imaging platform for cancer detection, Nano Lett. 17 (2017) 1648–1654, https://doi.org/10.1021/acs.nanolett.6b04865.
[80] L. Zhang, P. Zhu, T. Wan, H. Wang, Z. Mao, Glutamine coated titanium for synergistic sonodynamic and photothermal on tumor therapy upon targeted delivery, Front. Bioeng. Biotechnol. 11 (2023), https://doi.org/10.3389/fbioe.2023.1139426.
[81] Q. Zhang, D.K. Jeppesen, J.N. Higginbotham, J.L. Franklin, R.J. Coffey, Comprehensive isolation of extracellular vesicles and nanoparticles, Nat. Protoc. 18 (2023) 1462–1487, https://doi.org/10.1038/s41596-023-00811-0.
[82] H. Zhao, B. Zhao, L. Li, K. Ding, H. Xiao, C. Zheng, L. Sun, Z. Zhang, L. Wang, Biomimetic decoy inhibits tumor growth and lung metastasis by reversing the drawbacks of sonodynamic therapy, Adv. Healthc. Mater. 9 (2020) 1901335, https://doi.org/10.1002/adhm.201901335.